

**NASA
Technical
Paper
2657**

December 1986

Finite-Element Reentry Heat-Transfer Analysis of Space Shuttle Orbiter

William L. Ko,
Robert D. Quinn,
and Leslie Gong

NASA

**NASA
Technical
Paper
2657**

1986

Finite-Element Reentry Heat-Transfer Analysis of Space Shuttle Orbiter

William L. Ko,
Robert D. Quinn,
and Leslie Gong

*Ames Research Center
Dryden Flight Research Facility
Edwards, California*



National Aeronautics
and Space Administration

Scientific and Technical
Information Branch

SUMMARY

A structural performance and resizing (SPAR) finite-element thermal analysis computer program was used in the heat-transfer analysis of the space shuttle orbiter subjected to reentry aerodynamic heating. Three wing cross sections and one midfuselage cross section were selected for the thermal analysis. The predicted thermal protection system surface temperatures were found to agree well with flight-measured temperatures. The calculated aluminum structural temperatures also agreed reasonably well with the flight data from reentry to touchdown. The effects of internal radiation and internal convection were found to be significant. The SPAR finite-element solutions agreed reasonably well with those obtained from the conventional finite-difference method.

INTRODUCTION

The space shuttle orbiter reenters the earth atmosphere at an altitude of approximately 121,920 m (400,000 ft) and at extremely high velocity (nearly Mach 25). To protect the shuttle structure from severe reentry aerodynamic heating, the entire shuttle structure is covered with a thermal protection system (TPS). The regions of the shuttle surfaces that are subjected to lower heating rates--such as upper wing surfaces, fuselage sidewalls, and bay doors--are covered with highly flexible felt reusable surface insulation (FRSI). The regions exposed to higher heating rates--such as wing and fuselage lower surfaces--are covered with TPS tiles. A layer of highly flexible strain isolation pad (SIP) is sandwiched between the TPS tiles and the aluminum skin to absorb the strain incompatibility between the

brittle tiles and the skin. Overheating of the aluminum structure may cause thermal creep (which, in turn, could result in the loss of structural integrity that is required for subsequent flights). To some extent, the SIP layer may absorb the thermal buckling effect of the aluminum skin on the TPS tiles. However, excessive thermal buckling of the aluminum skin from overheating could cause a debonding of the TPS tiles. This, in turn, may result in partial or total loss of protection by the TPS.

In previous space transportation system (STS) shuttle flights, TPS performance was excellent. Hence, the shuttle structural temperatures during reentry were kept well below the design limit temperature of 176°C (350°F), and the aforementioned concerns were practically nonexistent. However, each shuttle is to be flown as many as 100 times. Therefore, an understanding of

mechanical performance, such as structural stress levels, under the reentry aerodynamic and thermal loadings is essential to establish shuttle structural integrity.

The flight load data obtained from onboard strain gauge measurements contain both the mechanical and the thermal components. Unfortunately, these two components cannot be practically separated experimentally. To obtain mechanical stresses, thermal stresses must be subtracted from the strain-gauge-measured stresses. This can be done analytically by first calculating the thermal stresses and then subtracting them from the strain-gauge-measured stresses to give the true mechanical stresses. To calculate thermal stresses, the structural temperature distribution must be known. The number of onboard thermocouples is insufficient to record accurately the structural temperature distribution. (Refer to the appendix.) Therefore, heat-transfer analysis must be performed to calculate accurate structural temperature distribution. The temperature distribution data thus obtained can be used as input to a structural model for thermal stress calculations.

Preliminary heat-transfer analyses of typical wing cross sections and a fuselage cross section were reported in references 1 to 3. The purpose of this report is to extend the previous work and perform finite-element heat-transfer analyses of three shuttle orbiter wing segments (WS) and one fuselage cross section (FS). The results will be compared with the STS-5 data, the most complete set of STS flight data obtained thus far. The work presented in this report can then be extended to a thermal analysis of the entire wing and fuselage.

NOMENCLATURE

A_i	surface area of radiation exchange element i
C	capacitance matrix
F_{ij}	radiation view factor, the fraction of radiant heat leaving radiation element i incident on radiation element j
FDT	factor for adjusting integration time step
FRSI	felt reusable surface insulation
FS	fuselage cross section
HRSI	high-temperature reusable surface insulation
JLOC	joint location or node
K_k	conduction matrix
K_r	radiation matrix
LRSI	low-temperature reusable surface insulation
Q	source heating load vector
R	radiation load vector
RI	time interval for radiation load vector computations
RTV	room-temperature vulcanized
SIP	strain isolation pad
SPAR	structural performance and resizing

SRU	unit of measurement of computer usage; the number of SRUs indicates the central processor time, memory, and input-output activities
STS	space transportation system
T	absolute temperature
THEOSKN	NASA theoretical thin-skin computer program
TPS	thermal protection system
t	time, sec
WS	wing segment or wing station
X,Y,Z	rectangular coordinate system
X	dimension along X axis, m (in.)
Y ₀	station on Y axis, m (in.)
[$\dot{}$]	$\frac{\partial[]}{\partial t}$
[$\ddot{}$]	$\frac{\partial^2[]}{\partial t^2}$
[\cdots]	$\frac{\partial^3[]}{\partial t^3}$

DESCRIPTION OF PROBLEM

Figure 1 shows three wing segments, WS240, WS328, and WS134, and one midfuselage cross section, FS877, selected for the heat-transfer analyses. Wing segment WS240 is bounded by WS240 and WS254; WS328 is bounded by WS328 and WS342.5 (fig. 1). Wing

segment WS134 includes a segment bounded by wing stations WS134 and WS147, part of the wheel well bounded by WS134 and WS160, and the glove area up to FS807 (fig. 1). The leading edge portion of the wing and the elevon were not included in the analysis.

The reentry trajectory for the space shuttle is shown in figure 2. The time is counted from the beginning of reentry, which occurs at an altitude of 121,920 m (400,000 ft). The nominal (or design) trajectories are indicated by solid curves, and measured data points are those obtained from the STS-5 flight. The trajectories for STS-1 through STS-4 are similar to the STS-5 flight trajectory. The calculation of reentry aerodynamic heatings is based on the actual STS-5 flight trajectory. The STS-5 flight was chosen because it provided the most complete set of flight data, as compared with other STS flights for which some data were lost.

DESCRIPTION OF STRUCTURES

Wing Segment WS240

The geometry of wing segment WS240, bounded by wing stations WS240 and WS254, is shown in figure 3. The upper and lower skins of bay 1 and the forward spar web of bay 1 are made of aluminum honeycomb-core sandwich panels. The upper and lower skins of bays 2 to 4 are made of hat-stringer-reinforced aluminum skins. The spar webs, except for the bay 1 forward spar web, are made of corrugated aluminum plates. The entire lower wing skin is covered with high-temperature reusable surface insulation (HRSI) tiles, with a SIP underlayer to absorb the strain

incompatibility between the skin and HRSI. Most of the upper skin of bay 1 is protected by low-temperature reusable surface insulation (LRSI) tiles, which overlay the SIP layer. A small portion of the upper skin of bay 1 and the upper skins of bays 2 to 4 are covered with highly flexible FRSI that has no SIP underlayer.

Wing Segment WS328

Wing segment WS328, bounded by wing stations WS328 and WS342.5 (fig. 4), has only three bays. The forward spar web of bay 1 is made of aluminum honeycomb-core sandwich panels; the remainder of the spar webs are corrugated aluminum plates. All the lower and upper aluminum skins are hat-stringer reinforced. The lower skin is protected with HRSI, and the upper skin with LRSI. No FRSI appears on the upper surface of WS328.

Wing Segment WS134

The geometry of wing segment WS134 is shown in figure 5. The lower and upper skins of bays 2 to 4, as well as those of the glove area, are made of hat-stringer-reinforced aluminum panels. The leading edge region of the glove and the upper skin of the wheel well (bay 1) are made of aluminum honeycomb-core sandwich structures. All the spar webs and the wheel well vertical walls are made of corrugated aluminum skins. The landing gear door is made of aluminum stringer-core-reinforced sandwich structure. The entire lower surface and the glove leading edge region of WS134 are covered with HRSI; most of the upper surface of WS134 is covered with FRSI, with small regions covered with HRSI and LRSI.

Fuselage Cross Section FS877

Fuselage cross section FS877 is shown in figure 6. The bottom and the sidewalls of the fuselage are made of T-stiffener-reinforced aluminum skins. The lower and upper glove skins (except for the leading edge region) are made of hat-stringer-reinforced aluminum skins. The leading edge region of the glove skin is made of aluminum honeycomb-core sandwich structures. The bay door is a sandwich structure made of Nomex (E.I. du Pont de Nemours & Co.) honeycomb-core and graphite-epoxy skins. A small portion of the bay door inner surface is covered with a layer of room-temperature vulcanized (RTV) rubber to serve as a heat sink. The fuselage bottom, lower glove, glove leading edge region, and part of the glove upper surface (near the leading edge region) are covered with HRSI. Most of the upper glove outer surface is covered with LRSI. The lower portion of the sidewall outer surface is covered with FRSI, and the upper portion with LRSI. The outer surface of the payload bay door is covered with a layer of FRSI.

THERMAL MODELING

Structural Simplifications

Because of the complex structure of the shuttle, some structural simplifications were necessary before the thermal models were set up, so that the analyses would be manageable with existing computers. Excessively detailed models could lead to tedious radiation view-factor computations, and the gain in the solution accuracies might be small in comparison to the solution obtained from simpler, yet reasonably detailed, models. To

examine the adequacy of representing the hat-stringer- and T-stiffener-reinforced skins with smooth skins of uniform equivalent thicknesses, the conventional finite-difference method was used in the two-dimensional heat-transfer analyses of a single hat stringer and a single T-stiffener. As shown in figure 7, the hat stringer that was analyzed was located on the lower skin of WS240 bay 3. The upper skin, the spar webs, and the lower skin (excluding the hat stringer) were assumed to have uniform effective thicknesses.

In the analyses, all types of radiation heat exchanges were considered: (1) external radiation from the TPS surface into space, (2) radiation exchanges between the hat-stringer outer surface and the inner surfaces of the bay, and (3) internal radiation inside the hat stringer. The heat input was based on Rockwell mission 3 heatings. The results shown in figure 8 give the peak temperature difference between points A and B on WS240 to be approximately 14.44°C (26°F). The temperature curves for the case of no internal radiation within the hat stringer almost coincided with the corresponding temperature curves for which the hat-stringer internal radiation was considered. This suggests that the effect of the hat-stringer internal radiation is negligible.

The T-stiffener that was analyzed was located at the bottom of FS877, as shown in the inset of figure 9. In this case, only the external radiation from the TPS surface into space was considered, and the internal radiation from the T-stiffener into the fuselage inner wall was neglected. The temperatures at points A, B, and C of the

T-stiffener (fig. 9) differ only slightly. The temperature differences between points A and B of the hat-stringer and the T-stiffener are negligible. Therefore, in the finite-element thermal modeling, the hat-stringer- and T-stiffener-reinforced skins, the corrugated spar webs, and the honeycomb-core sandwich skins and spar webs are represented by smooth solid skins with effective thicknesses.

Finite-Element Models

Several finite-element models were set up for the SPAR (ref. 4) finite-element heat-transfer analyses of the shuttle. Wing segment WS240 was the most extensively analyzed because most of the instrumentation for gathering structural temperature data existed at station WS240. WS240 was modeled in one, two, and three dimensions. Both WS328 and WS134 were modeled in three dimensions only; fuselage cross section FS877 was modeled in two dimensions. The structural models for thermal stress calculations do not include the secondary load-carrying structures--the elevon and leading edge region of the wing. Hence, in all thermal modelings for the entire wing cross sections, these secondary load-carrying regions were neglected.

Because of the presence of gaps between the TPS tiles (HRSI and LRSI), the heat flow through the TPS tiles was restricted only in the thickness direction of the tiles for all thermal models described below. In the analyses, two TPS thicknesses (80 and 100 percent) were used for both the HRSI and the LRSI tiles. The purpose of using the effective thickness of 80 percent of the original TPS thickness was to account for the gap

heatings between the TPS tiles. The effect of internal natural convective heat transfer was neglected. (At present, the capability of handling two-dimensional free convection is being introduced to the SPAR program.) The effect of the external forced convective coolings (negative heatings) on the structural temperatures near the end of the flight was found to be negligible and therefore was neglected for all thermal models except WS240 three-dimensional and WS328 three-dimensional models. The thermal properties for input to the SPAR thermal models were obtained from the manufacturers. The temperature and pressure (or time) dependencies of the TPS thermal properties are as follows: reusable surface insulation (RSI) coating--a function of temperature only; RTV--a constant; and HRSI, LRSI, FRSI, and SIP--functions of both temperature and pressure (or time).

One-dimensional wing model- The one-dimensional thermal model set up for WS240 bay 3 is shown in figure 10. This model was used to examine the variation of solutions obtained by modeling the HRSI in 5, 10, and 15 layers. All the aluminum skins, as well as HRSI, FRSI, SIP, and RTV, were modeled with K41 (four-node heat-conduction) elements. The aerodynamic surfaces were modeled with K21 (two-node heat-conduction) elements of unit cross section for source heat generation. The internal and external radiation effects were modeled by attaching R21 (two-node radiation) elements at the radiation surfaces of the aluminum skins and the TPS. The vertical sides of all K41 elements were insulated. The radiation into space was modeled with only one R21 element that was kept at a constant temperature of 26.67°C (80°F). As discussed later, division

of the lower TPS into 10 or more sublayers gave sufficiently accurate solutions. Therefore, in setting up all other thermal models, the lower TPS was modeled in 10 or more sublayers, and the upper TPS in 3 to 5 sublayers. The one-dimensional model was also used to compare the SPAR finite-element solution with that obtained from the conventional finite-difference method.

Two-dimensional wing models- Two-dimensional SPAR thermal models were set up for two cases: the two-dimensional one-cell model for WS240 bay 3 (fig. 11), and the two-dimensional model for the entire WS240 load-carrying cross section excluding the leading edge region and the elevon (fig. 12). The two-dimensional one-cell model was used to study the effects of the existence of spar webs and chordwise heat flows (within bay 3) through the aluminum skins. The two-dimensional model was used to examine the effect of the other bays. The aluminum skins and spar webs were modeled with K21 elements rather than K41 elements, as in the case of the one-dimensional model. However, the HRSI, SIP, RTV, and FRSI were modeled with K41 elements. The K21 elements of unit cross section were used to model the aerodynamic surfaces for source heat generation. The radiation surfaces and the radiation into space were modeled with R21 elements. The front and rear portions of the models were insulated. The two-dimensional one-cell model has 123 joint locations (JLOCs) or nodes, and the WS240 two-dimensional model has 383 JLOCs.

Three-dimensional wing models- The three-dimensional models are capable of handling the effects of chordwise and spanwise heat flows and the

effect of the existence of rib trusses. Two types of SPAR three-dimensional models were set up for WS240: the three-dimensional one-cell model with 268 JLOCs (fig. 13) and the three-dimensional wing segment model with 920 JLOCs (fig. 14). The wing skins, spar webs, rib-cap shear webs, RTV layers (on both sides of SIP), and TPS surface coatings were modeled with K41 elements. The spar caps, rib caps, and rib trusses were modeled with K21 elements. The TPS was modeled in 10 sublayers on the lower surface, and 3 to 4 sublayers on the upper surface using K81 (eight-node three-dimensional heat-conduction) elements and K61 (six-node three-dimensional heat-conduction) elements. The K61 elements were used only in the region where the modeled TPS sublayers changed from four to three sublayers on the upper surface of WS240 bay 1 (fig. 14). The SIP was modeled with only one layer of K81 elements. The aerodynamic surfaces were modeled using one layer of K41 elements of unit thickness to provide source heat generation. The external and internal radiations were modeled by attaching a layer of R41 (four-node radiation) elements to the radiation surfaces. The radiation into space was modeled by one R41 element. No radiation elements were attached to the surfaces of the rib-cap shear webs and the rib trusses, because the exposed areas were small. The front and rear portions of the two SPAR three-dimensional models were totally insulated. The three-dimensional one-cell model was also used to study the effect of internal radiations.

SPAR modeling of WS328 was similar to that of the WS240 three-dimensional model. The lower TPS (HRSI) was modeled in 13 sublayers, and the upper TPS (LRSI) in 5 sublayers. The WS328

three-dimensional model shown in figure 15 had a total of 916 JLOCs.

The three-dimensional SPAR thermal model set up for WS134 is shown in figure 16. The HRSI was modeled in 13 sublayers, and the LRSI in 3 sublayers. The landing gear was modeled with one K81 element to represent the large mass of the landing gear system. The remainder of the WS134 modeling is similar to that of the WS240 three-dimensional model. The WS134 three-dimensional model had 2075 JLOCs.

Two-dimensional fuselage model-

The SPAR model for FS877 was two dimensional (fig. 17) and had 605 JLOCs. Because of symmetry, only half of the fuselage cross section was modeled. The T-stiffener- and hat-stringer-reinforced skins were represented as smooth skins of effective thicknesses. The effective skins, glove honeycomb-core sandwich skins, bay door composite skins, longerons, vertical wall between the two longerons, torque box, and top centerline beam were modeled with K21 elements. The glove aluminum honeycomb core was modeled with K41 elements having effective thermal properties. The bay door of Nomex honeycomb core was modeled by using both K41 and K31 (three-node heat-conduction) elements having effective conduction properties. The TPS everywhere was modeled in 10 sublayers with K41 elements.

AERODYNAMIC HEATING

The external heat inputs to the thermal models were computed by a NASA theoretical thin-skin computer program called THEOSKN, using the velocity, altitude, and angle-of-attack time

histories of the flight-measured STS-5 shuttle trajectory given in figure 2. The THEOSKN computer program solves the one-dimensional thin-skin heating equation and computes time histories of surface temperatures, heating rates, heat-transfer coefficients, and skin friction. The thermodynamic and transport properties of air used in this analysis are given in reference 5.

Representative heating rates for WS240, WS328, and WS134 are given in figures 18, 19, and 20, respectively. The heating rates for the lower surfaces were computed assuming laminar flow up to 1160 sec and turbulent flow from 1160 sec until the end of the flight. The laminar heat transfer was computed by relating heat transfer to a skin friction equation through a modified Reynolds analogy. In this analysis, the Blasius incompressible skin friction equation (ref. 6) was related to heat transfer by the Prandtl number to the -0.6 power. Compressibility effects were accounted for by using the Eckert reference enthalpy transformation (ref. 7). Details of this method for calculating heat transfer at hypersonic speeds are given in reference 8. The turbulent heat transfer was computed by a similar procedure except that the Van Driest transformation (refs. 9 and 10) was used to account for compressibility and the Reynolds analogy factor was assumed to be a constant value of 1.1.

The boundary-layer flow on the upper surface of bay 1 for both WS328 and WS240 was assumed to be attached. The remainder of the upper wing surface was assumed to be in a region of separated flow. The heat transfer for the attached flow areas was computed using the same heat-transfer codes used to calculate the lower surface heating.

To calculate the heating rates for the separated flow areas on the upper surface, the heat-transfer codes were empirically modified. The empirical corrections were determined from comparisons with previously measured flight data.

Heating rates calculated for FS877 are shown in figure 21 for six typical locations. The transition from laminar to turbulent heating occurred at time t equal to 1100 sec. The laminar heat transfer for the lower fuselage and leading edge of the glove were calculated using the infinite swept-cylinder theory, together with the heat-transfer theories of Fay and Riddell (ref. 11) and Lees (ref. 12). The heat transfer on the lower glove was increased by 20 percent, as suggested by wind-tunnel test results. The turbulent heat-transfer coefficients were computed by the method given in reference 13. The heating rates for the upper fuselage were calculated using empirical relationships derived from comparisons between calculated surface temperatures and measured data obtained from previous shuttle flights.

RADIATION EXCHANGE

For both external and internal thermal radiation exchanges, all the view factors that were calculated obey the following equation (ref. 14):

$$A_i F_{ij} = A_j F_{ji} \quad (1)$$

where A_i is the surface area of radiation exchange element i and F_{ij} is the radiation view factor, defined as the fraction of radiant heat leaving element i incident on element j . In calculating view factors for the

external radiation exchanges where element i represents the space element and element j any radiation exchange element on the wing or fuselage surface, F_{ij} was assumed to be unity. Therefore, according to equation (1), $F_{ji} = A_i/A_j$.

In the view-factor calculations for fuselage internal radiation exchanges, each radiation exchange element was set to receive radiation not only from the other elements but also from mirror images of all elements. In other words, the entire fuselage cross section was used to compute the fuselage internal radiation view factors. Values of emissivity and reflectivity used to compute radiant heat fluxes are as follows:

<u>Surface</u>	<u>Emissivity</u>	<u>Reflectivity</u>
Windward	0.850	0.150
Leeward	0.800	0.200
Internal structure	0.667	0.333
Space	1.000	0

The initial temperature distribution used in the analysis was obtained from actual flight data. In thermal modeling, most of the time was consumed in computing the view factors.

TRANSIENT THERMAL SOLUTIONS

The SPAR thermal analysis finite-element computer program was used in the calculation of temperature-time histories at all joint locations of the thermal models. The SPAR program used the following approach to obtain transient thermal solutions.

The transient heat-transfer matrix equation that was used is of the form

$$(K_k + K_r)T + C\dot{T} = Q + R \quad (2)$$

where

C	capacitance matrix
K_k	conduction matrix
K_r	radiation matrix
Q	source heating load vector
R	radiation load vector
T	absolute temperature

$$[\dot{}] \equiv \frac{\partial[]}{\partial t}$$

$$[\ddot{}] \equiv \frac{\partial^2[]}{\partial t^2}$$

$$[\dddot{}] \equiv \frac{\partial^3[]}{\partial t^3}$$

Equation (2) was integrated by assuming that the temperature vector T_{i+1} at time step t_{i+1} can be expressed in Taylor series as

$$T_{i+1} = T_i + \dot{T}_i \Delta t + \frac{1}{2!} \ddot{T}_i \Delta t^2 + \frac{1}{3!} \dddot{T}_i \Delta t^3 + \dots \quad (3)$$

where T_i is the temperature vector at time step t_i and Δt is the time increment. The vector \dot{T}_i is obtained directly from equation (2):

$$\dot{T}_i = -C^{-1}(K_k + K_r)T_i + C^{-1}(Q + R) \quad (4)$$

Higher order derivatives are obtained by differentiating equation (2) according to the assumption that material properties and R are constant over Δt and that Q varies linearly with time. Hence,

$$\ddot{T}_i = -C^{-1}(K_k + 4K_r)\dot{T}_i + C^{-1}\dot{Q} \quad (5)$$

$$\ddot{\ddot{T}}_i = -C^{-1}(K_k + 4K_r)\ddot{T}_i + 4\dot{K}_r\dot{T}_i \quad (6)$$

The SPAR program automatically calculates the integration time step Δt internally. However, if the solution does not converge, Δt can be adjusted by using reset command FDT.

In the present computations, the Taylor series expansion given in equation (3) was cut off after the third term. The pressure dependency of the TPS and SIP thermal properties was converted into time dependency based on the trajectory given in figure 2.

Time-dependent properties were averaged over RESET TIME (or time intervals), which was taken to be 2 or 25 sec. Temperature-dependent properties were evaluated at the temperatures computed at the beginning of each time interval. The values of Q , \dot{Q} , and R were computed every 2 sec.

RESULTS

TPS Sublayers

Figure 22 shows the lower aluminum skin temperatures predicted from the WS240 one-dimensional model (fig. 10) for which the HRSI (lower TPS) was modeled in 5, 10, and 15 sublayers.

Mission 3 heating data were used in this study. The temperature curves for 5, 10, and 15 TPS sublayers are very close, with a maximum temperature difference of only 1.67°C (3.01°F). In figure 23, peak skin temperatures for the three cases are plotted against the number of TPS sublayers. HRSI modeling of more than 10 sublayers is seen to give sufficiently accurate temperature solutions. The time histories of the temperature distributions (using Rockwell-calculated surface heating) within the HRSI of the WS240 three-dimensional model are shown in figure 24. The maximum temperature differences between the outer and inner surfaces for the HRSI and the FRSI occurred at 1000 sec and 500 sec, respectively, from reentry.

Effect of Internal Radiation

The effect of the internal radiation (radiation inside the bay) was investigated using the WS240 three-dimensional model (fig. 13) and assuming total insulation on the outer surfaces of the spar webs. The results shown in figure 25 are for mission 3 heatings. When the effect of internal radiation was considered, the lower and the upper skin temperatures were brought closer together (especially after landing), and the peak lower skin temperature was reduced by approximately 39°C (70°F).

Comparison of Solutions

Figure 26 shows WS240 bay 3 aluminum skin temperatures calculated using different thermal models for WS240. Mission 3 heatings were used in the temperature calculations. By introducing the effects of spar webs and

neighboring bays (that is, by extending the one-dimensional model in fig. 10 to the two-dimensional model in fig. 12), the lower and upper skin peak temperatures (predicted from the one-dimensional model) were reduced by approximately 8.89°C (16°F) and 17.78°C (32°F), respectively. By extending the two-dimensional model (fig. 12) to the final three-dimensional wing segment model in figure 14 (that is, by adding the effect of rib trusses and the effect of spanwise heat flows), the lower and upper skin peak temperatures were further decreased by 8.33°C (15°F) and 12.22°C (22°F), respectively. Thus, the total reductions of the lower and upper skin peak temperatures were 17.22°C (31°F) and 30°C (54°F), respectively, when extending the one-dimensional model to the final three-dimensional model for WS240. This demonstrates that the three-dimensional model gave more accurate solutions than one- and two-dimensional models. In figure 26, the temperature predicted from the three-dimensional one-cell model was slightly higher than that predicted from the three-dimensional wing segment model for WS240. This could be due to the combined effects of spanwise and chordwise heat flows and the effect of the trusses.

TPS Surface Temperatures

In figures 27 to 30, the predicted and the STS-5 flight-measured TPS surface temperatures are compared for WS240, WS328, WS134, and FS877. (Thermocouple locations are shown in the appendix, figures 43 to 46.) The data are in good agreement, which indicates that the calculations of the aerodynamic heatings were satisfactory. As expected, the lower TPS surface

temperatures of WS134 (inboard station) are slightly lower than those of two outboard stations (WS240 and WS328) because flow distances from the stagnation point for WS134 are longer than those for WS240 and WS328. In a narrow time range of $t = 1500$ to 2000 sec (immediately before and after touchdown time), the flight data--especially for the lower TPS surfaces--gave lower temperatures than those calculated. This discrepancy could have been caused by insufficient forced convective coolings in the heat input calculations and the neglect of internal convection that resulted primarily from cool air entering the shuttle. (Air enters the interior of the shuttle orbiter at 30,480-m (100,000-ft) altitude, about 1400 sec from reentry.)

Using forced convective cooling near the touchdown time (negative heating) resulted in excess computation time because of a change of sign in heat input. However, the effect of such negative heating on the structural temperatures was almost inconspicuous when plotted. Therefore, negative heating was not included in the thermal analyses of WS134 and FS877. The flight data for the lower TPS surfaces of WS240 bay 3 (fig. 27) and WS134 bay 1 (fig. 29) contain void data because the lower limits of the thermocouple temperature readouts were set too high. The measured temperatures for the FS877 bottom TPS surface at JLOC97 shifted slightly upward with time.

Structural Temperatures

Figures 31 to 34 compare the STS-5 flight data with the computed aluminum skin temperatures at typical points on WS240, WS328, WS134, and FS877,

respectively. The temperature calculations were made using 80- and 100-percent TPS thicknesses. For the WS240 (fig. 31), the measured lower skin temperature data closely followed the calculated temperature curves for 100-percent TPS thickness almost up to touchdown time. After that, the flight temperature data were consistently lower. The marked discrepancies between the calculated and measured lower skin temperatures after touchdown could have been caused by the effect of internal convective cooling resulting from outside air entering the wing interior. The effect of internal free convections was neglected because at the time of the analysis the SPAR program was not capable of calculating free convective heat transfer. For the upper skin of WS240, the measured and calculated temperatures (based on 100-percent TPS thickness) compared reasonably well even after touchdown. The agreement was especially good for the bay 1 upper skin.

For the lower skins for both WS328 and WS134 (figs. 32 and 33, respectively), the flight data tended to follow the predicted temperature curves based on 80-percent TPS thickness during reentry (up to 1600 sec). Then the data deviated from the predicted temperature curves. This indicates the effects of gap heating during reentry and the internal convective cooling inside the wing, which began shortly before touchdown. For the upper skins of both WS328 and WS134, the effect of gap heating was not observed. The data correlated fairly well with the predicted temperature curves based on 100-percent TPS thickness.

In figure 34, the calculated structural temperatures for FS877 are compared with STS-5 flight-measured

data. During reentry, the flight data compared reasonably well with the calculated temperatures based on 100-percent TPS thickness, except for JLOC108. Again, the convection inside the fuselage caused by the entering of outside air resulted in lower measured temperature values after $t = 1700$ sec.

Figures 35 to 37 show the chord-wise distributions of aluminum skin temperatures at WS240, WS328, and WS134, respectively, for a reentry time of $t = 1600$ sec. The scalloped shape of the data curves reflects the temperature drop at the heat sinks or spar caps. The scalloped data points for the skin temperatures are in direct correlation to the degree of thermal stress buildups in the structure. With few exceptions, the STS-5 flight data correlated reasonably well with the predictions. The circumferential distribution of the FS877 structural temperatures is shown in figure 38. The "valleys" of the temperature profiles indicate temperature drops at the heat sinks or structural junction points. The payload bay outer skin was heated more than the sidewall, although the heat input there was relatively low. This indicates the poor heat conduction in bay door materials.

Finite-Element Method Compared With Finite-Difference Method

WS240 one-dimensional and two-dimensional one-cell models were used to compare the solutions obtained from the SPAR finite-element method and the conventional finite-difference method. The finite-difference models were made as close to the SPAR models as possible. As shown in figures 39 and 40, the solutions obtained from the two methods are similar. The SPAR

solutions tended to give slightly higher temperatures at point A on the lower skins for the two models studied. For the upper skins, the SPAR one-dimensional model (fig. 39) resulted in slightly lower temperatures. The temperatures at points B and C of the SPAR two-dimensional one-cell model (fig. 40) increased more rapidly than those predicted by the finite-difference method.

SPAR Solution Accuracy

A WS240 three-dimensional one-cell model was used to study the accuracy of the SPAR finite-element solutions. The RESET TIME, or the time interval for updating the time-dependent thermal properties, was set at 2, 25, 50, and 100 sec. The factor for adjusting integration time step (FDT) was 0.5, and the time interval for radiation load vector computations (RI) was 2.0 sec. The temperatures at point A of the lower skin are plotted in figure 41. The three solutions, each based on a different RESET TIME, are quite close. Figure 42 shows the plots of computer SRU units compared with SPAR RESET TIME. An SRU is defined as a unit of measurement of computer system usage. The number of SRUs indicates the central processor time, memory, and input-output activity. The solid curve in figure 42 is for the case in which the TPS was modeled with K81 elements and the heat flow was restricted in the TPS thickness direction. The dotted curve is for the case in which the TPS was represented by K21 elements oriented in the TPS thickness direction. By using K21 elements, the SRUs were reduced by about 20 percent. By increasing the RESET TIME from 2 sec to 25 sec, the reduction in SRUs was quite large (down 25 percent). A

further increase in RESET TIME showed very little gain (reduction in SRU). The solutions based on RESET TIME values of 2 and 25 sec (fig. 41) are graphically indistinguishable. Hence, by using a RESET TIME of 25 sec, the computer running cost can be greatly reduced while achieving a sufficiently accurate solution.

CONCLUSIONS

The finite-element computer program for structural performance and resizing (SPAR) was used in the reentry heat-transfer analysis of three wing segments and one midfuselage cross section of the space shuttle orbiter. The thermal models were set up in one, two, and three dimensions. The thermal analyses yielded the following results.

1. The predicted surface temperatures for the thermal protection system agreed favorably with the flight-measured data. Therefore, the "reference enthalpy method" can be used to predict reliable laminar heat-transfer coefficients at hypersonic speeds. Also, the Van Driest theory using a Reynolds analogy factor of 1.1 can be employed to predict reliable turbulent heat transfer at hypersonic and supersonic speeds. The measured temperatures showed that transition from laminar to turbulent flow over the entire analyzed wing surfaces occurred 1160 sec after reentry.

2. The measured and predicted structural temperatures correlated well prior to touchdown. This implies that the SPAR thermal models for both the wing segments and the fuselage cross section were adequate.

3. The internal convection was believed to have considerable effect on the structural temperatures after touchdown (especially for the fuselage) and cannot be neglected.

4. The effect of the internal radiation was found to be significant and cannot be neglected even at relatively low structural temperatures. The view-factor computations for the internal radiation were a major task in thermal analysis. Therefore, introducing the capability of automatic view-factor computations into the SPAR program is highly recommended.

5. In SPAR thermal modeling of the TPS for restricted one-dimensional heat flow, using K21 (two-node heat-conducting) elements was found to be more efficient (less computation time) than using K81 (eight-node) elements with heat flow permitted only in one direction. A RESET TIME (time interval for updating the time-dependent thermal

properties) of less than 25 sec did not improve the solution accuracy significantly but substantially increased the computer time.

6. Solutions obtained from the SPAR finite-element method and the conventional finite-difference method are in good agreement.

APPENDIX--THERMOCOUPLE LOCATIONS

Thermocouple locations for wing segments WS240, WS328, and WS134 and for fuselage cross section FS877 are shown in figures 43 to 46.

Ames Research Center
Dryden Flight Research Facility
National Aeronautics and Space
Administration
Edwards, California, March 23, 1984

REFERENCES

1. Ko, William L.; Quinn, Robert D.; Gong, Leslie; Schuster, Lawrence S.; and Gonzales, David: Preflight Reentry Heat Transfer Analysis of Space Shuttle. AIAA Paper 81-2382, Nov. 1981.
2. Ko, William L.; Quinn, Robert D.; Gong, Leslie; Schuster, Lawrence S.; and Gonzales, David: Reentry Heat Transfer Analysis of the Space Shuttle Orbiter. NASA CP-2216, 1982, pp. 295-325.
3. Gong, Leslie; Quinn, Robert D.; and Ko, William L.: Reentry Heating Analysis of Space Shuttle With Comparison of Flight Data. NASA CP-2216, 1982, pp. 271-294.
4. Marlowe, M. B.; Moore, R. A.; and Whetstone, W. D.: SPAR Thermal Analysis Processors Manual, System Level 16. NASA CR-159162, vol. 1, 1979.
5. Hansen, C. Frederick: Approximations for the Thermodynamic and Transport Properties of High Temperature Air. NASA TR R-50, 1959.
6. Schlichting, Hermann (J. Kestin, transl.): Boundary Layer Theory. Fourth ed. McGraw-Hill Book Co., Inc., New York, 1960.
7. Eckert, Ernst R. G.: Survey of Boundary Layer Heat Transfer at High Velocities and High Temperatures. WADC TR-59-624, Wright-Patterson AFB, Ohio, 1960.
8. Zoby, E. V.; Moss, J. N.; and Sutton, K.: Approximate Convective-Heating Equations for Hypersonic Flows. J. Spacecraft and Rockets, vol. 18, no. 1, Jan./Feb. 1981, pp. 64-70.
9. Van Driest, E. R.: The Problem of Aerodynamic Heating. Aeronaut. Engr. Rev., vol. 15, no. 10, Oct. 1956, pp. 26-41.
10. Hopkins, Edward J.; Keener, Earl R.; and Louie, Pearl T.: Direct Measurements of Turbulent Skin Friction on a Nonadiabatic Flat Plate at Mach Number 6.5 and Comparisons With Eight Theories. NASA TN D-5675, 1970.
11. Fay, J. A.; and Riddell, F. R.: Theory of Stagnation Point Heat Transfer in Dissociated Air. J. Aeronaut. Sci., vol. 25, no. 2, Feb. 1958, pp. 73-85, 121.
12. Lees, L.: Laminar Heat Transfer Over Blunt-Nosed Bodies at Hypersonic Flight Speeds. Jet Propulsion, vol. 26, no. 4, Apr. 1956, pp. 259-269.
13. Beckwith, Ivan E.; and Gallagher, James J.: Local Heat Transfer and Recovery Temperatures on a Yawed Cylinder at a Mach Number of 4.15 and High Reynolds Numbers. NASA TR R-104, 1961.
14. Sparrow, Ephraim M.; and Cess, R. D.: Radiation Heat Transfer. Augmented ed. Hemisphere Publication Corp., Washington, DC, 1978.

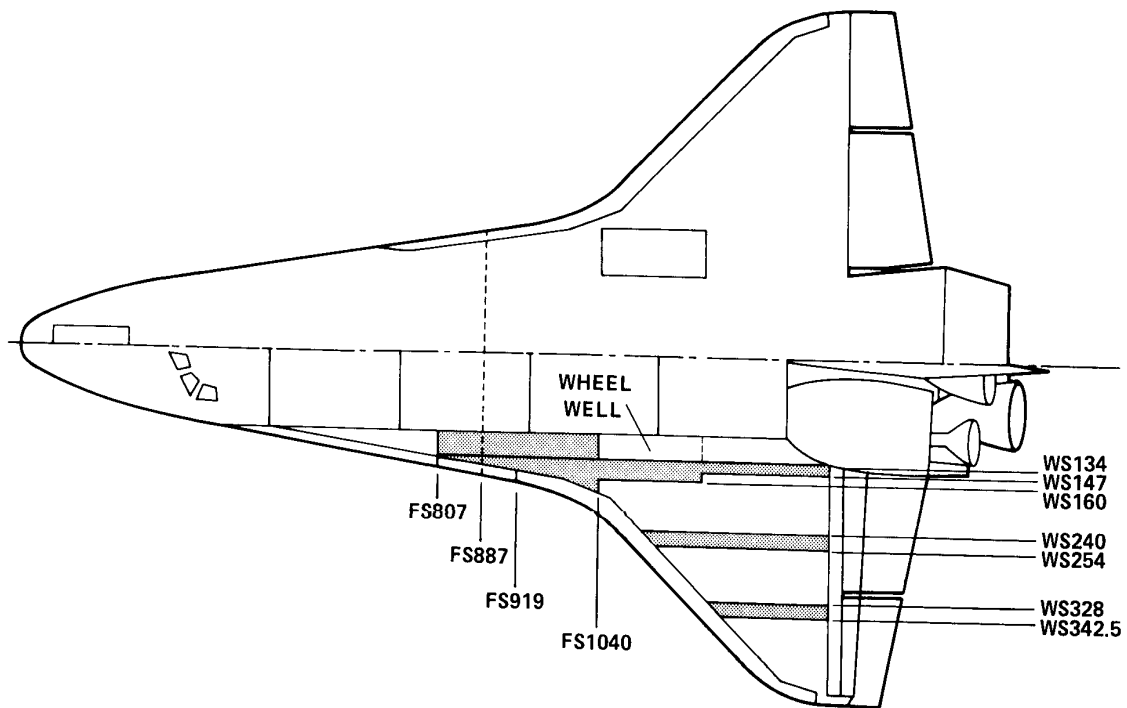


Figure 1. Location of space shuttle wing segments and fuselage cross section used in heat-transfer analysis.

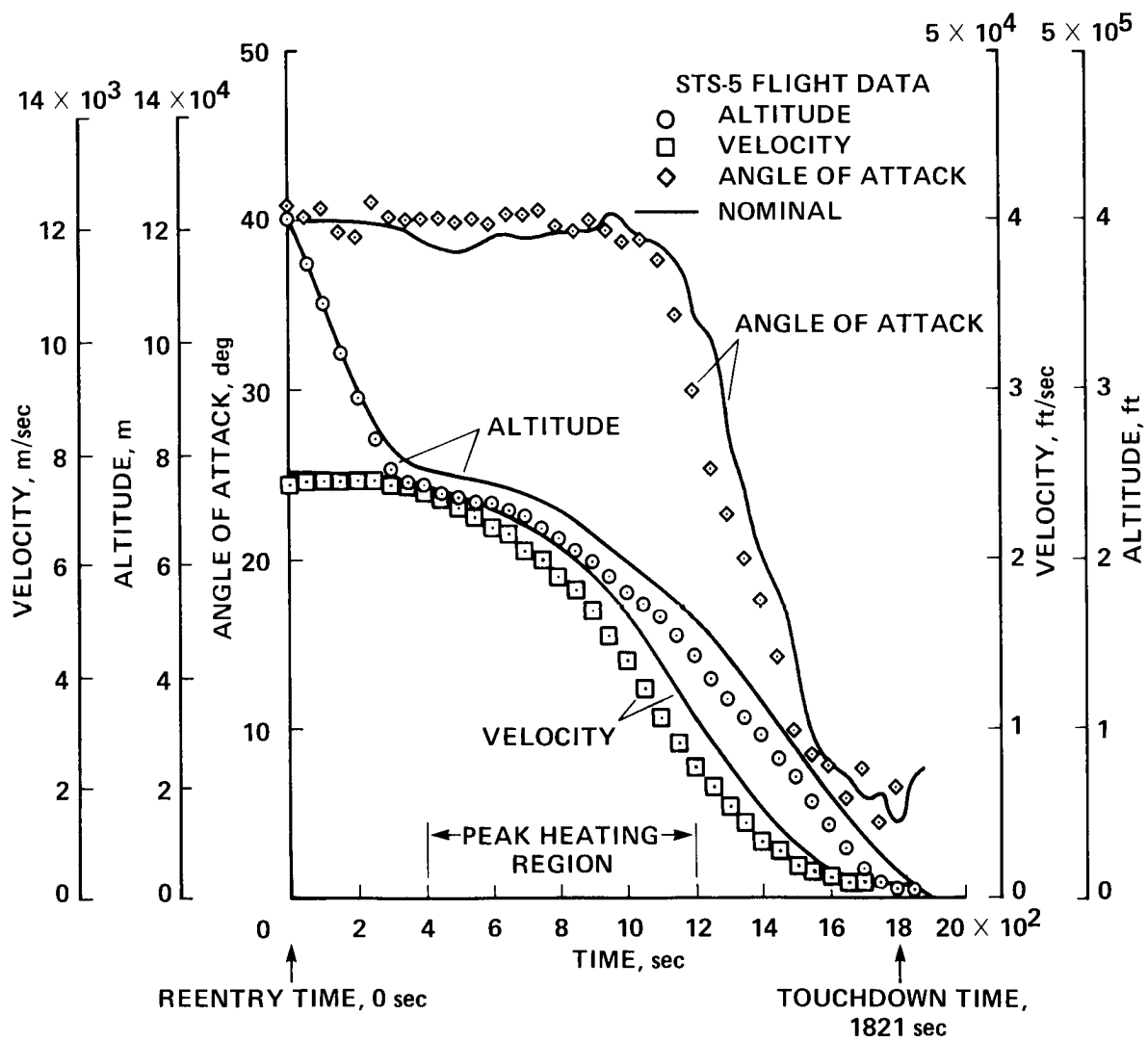


Figure 2. Reentry trajectory for STS-5.

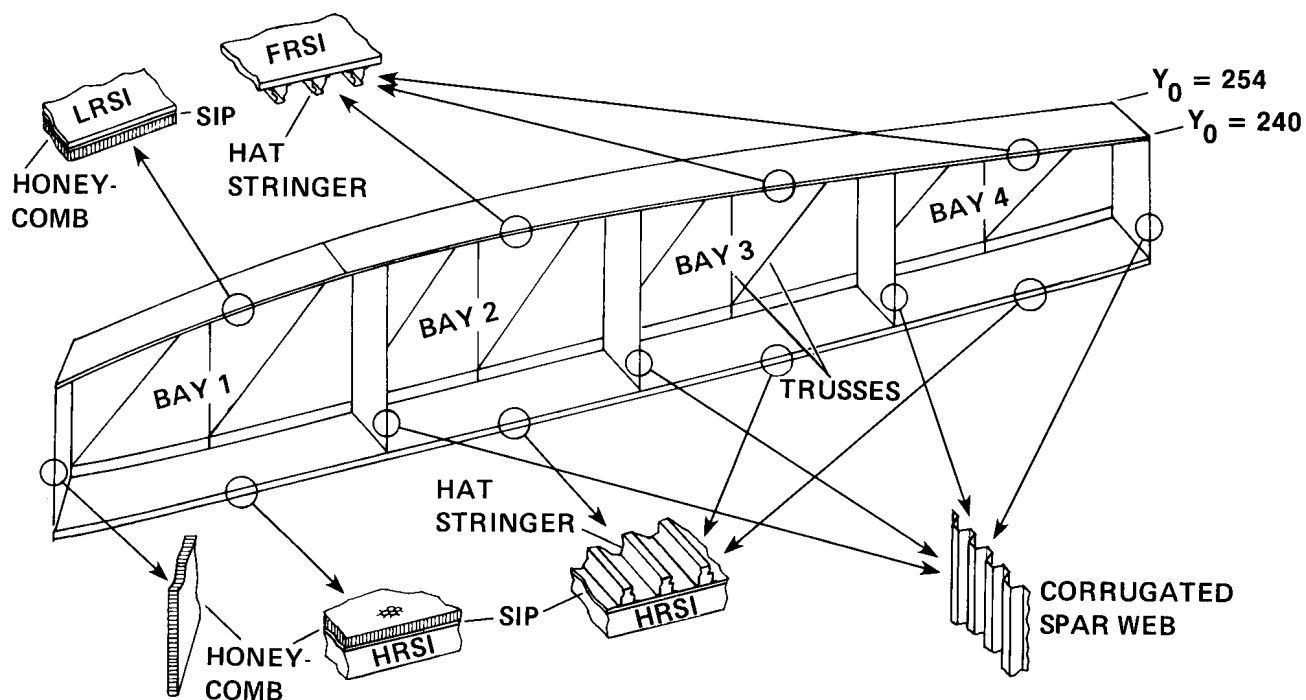


Figure 3. Geometry of wing segment WS240 between wing stations WS240 and WS254.

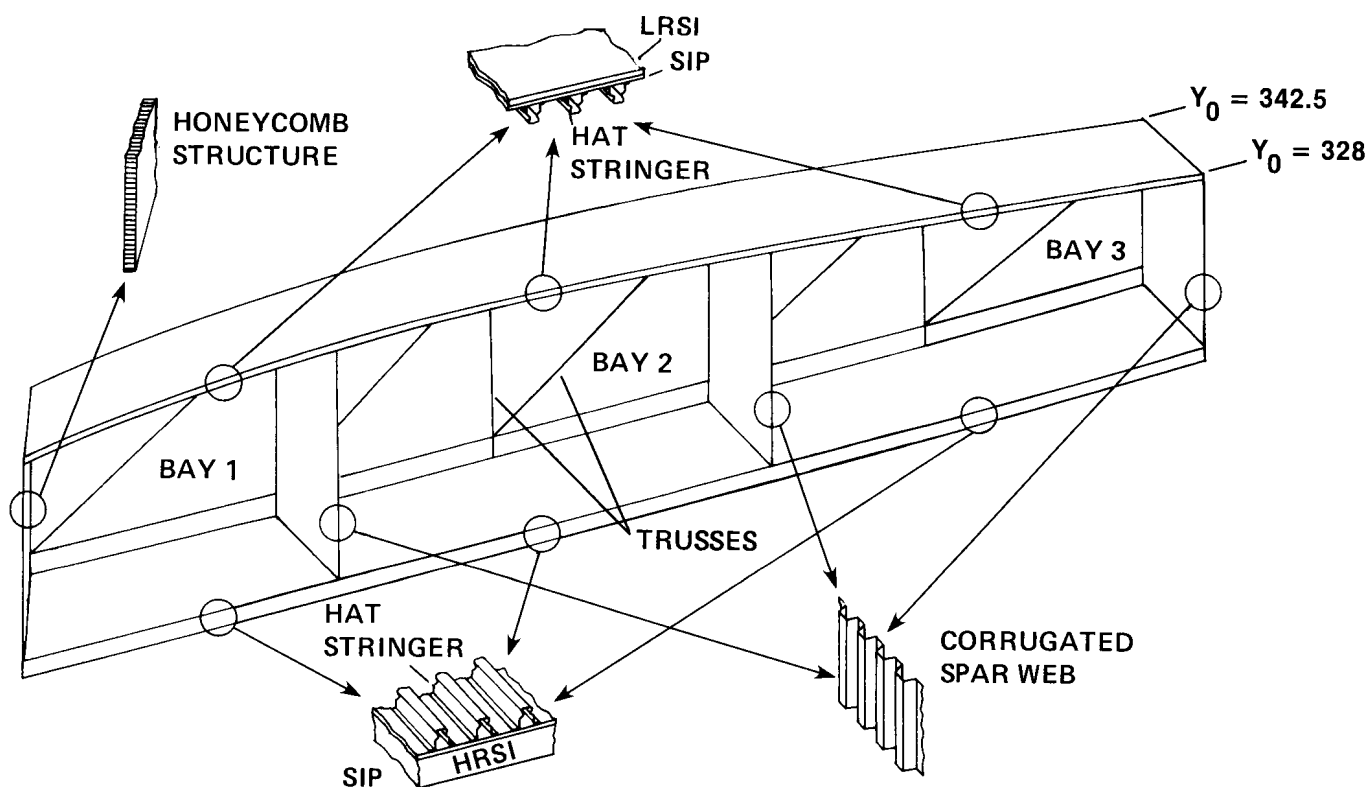


Figure 4. Geometry of wing segment WS328 between wing stations WS328 and WS342.5.

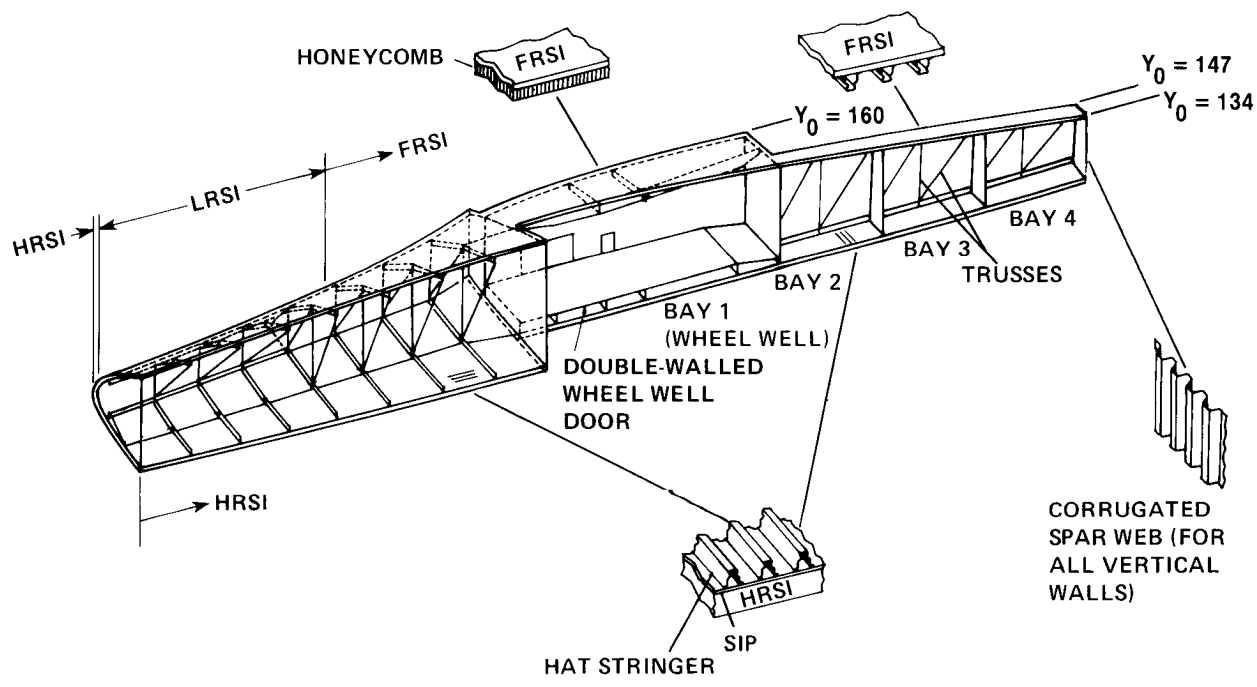


Figure 5. Geometry of wing segment WS134.

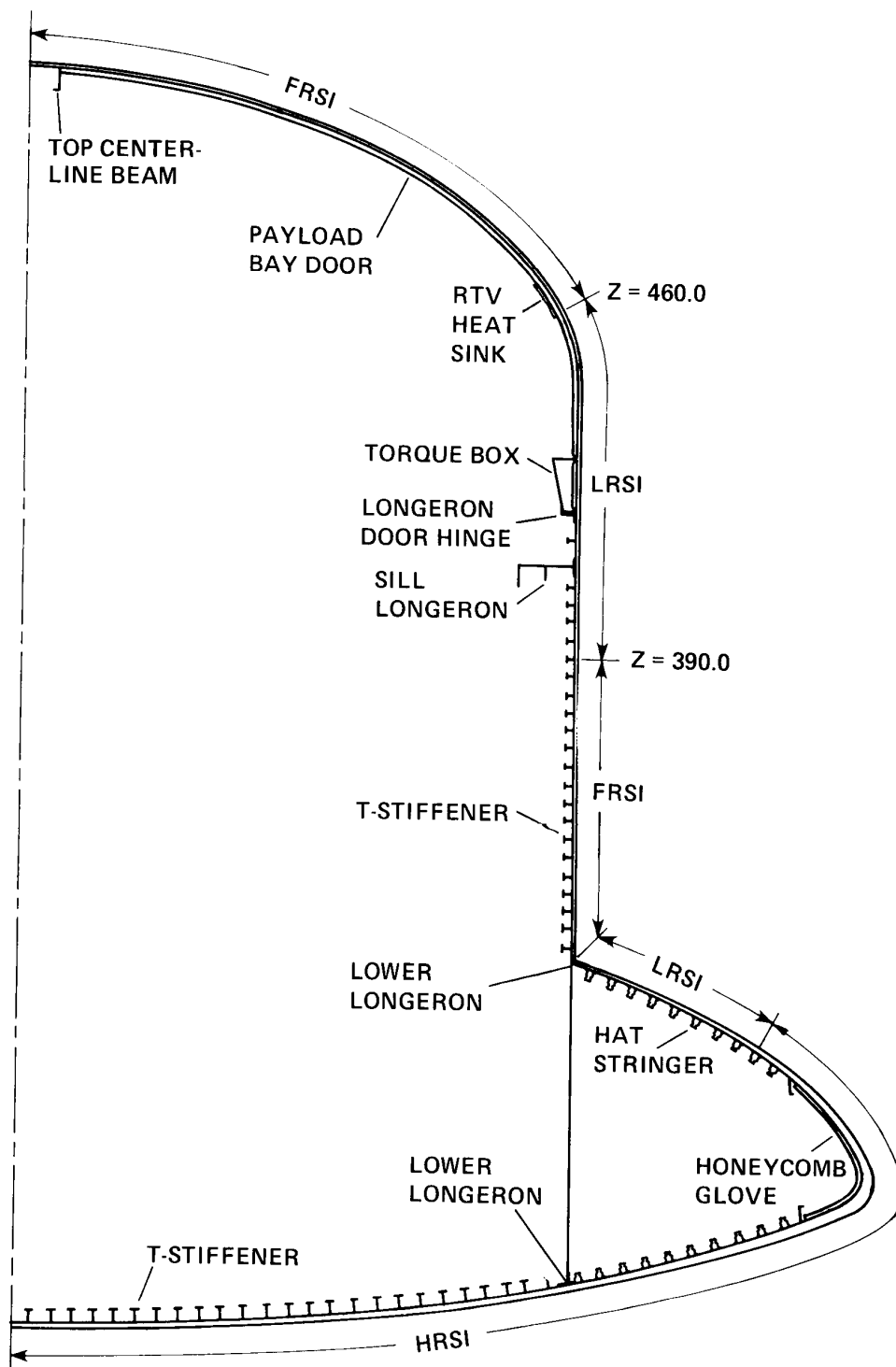


Figure 6. Geometry of fuselage cross section FS877.

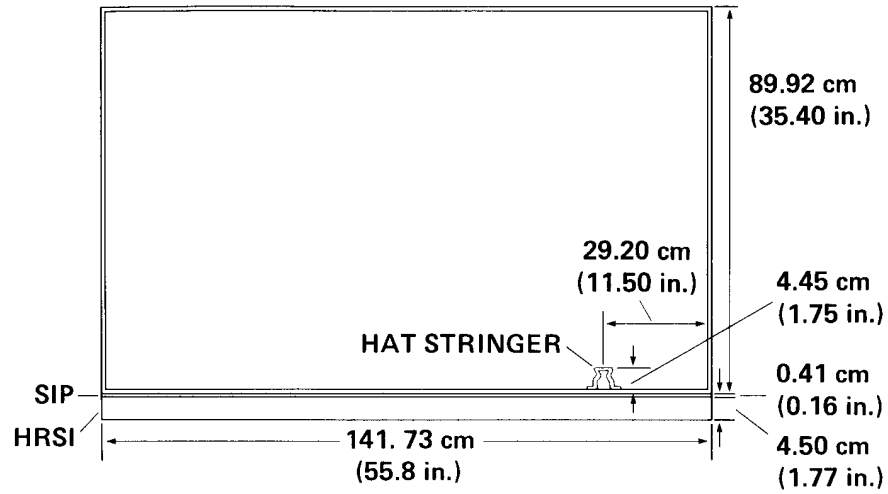


Figure 7. Wing segment WS240 bay 3 with one hat stringer.

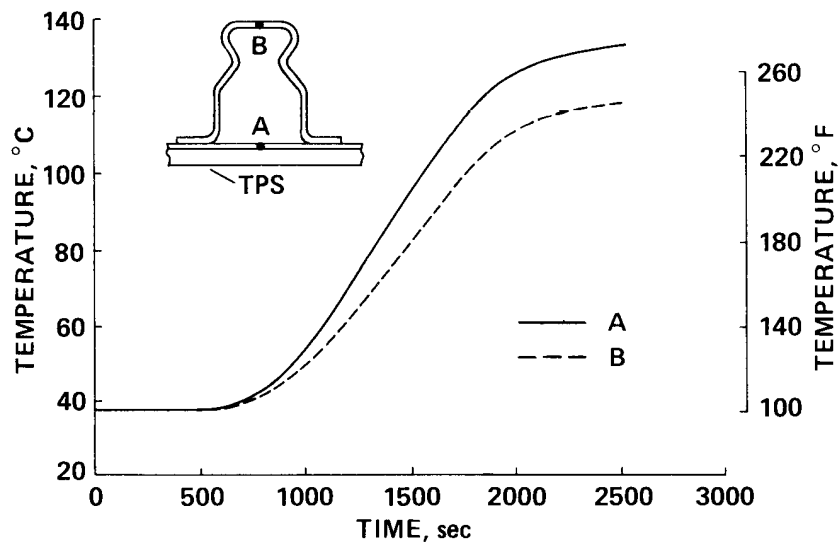


Figure 8. Temperature time histories at points in hat stringer on lower skin of WS240 bay 3 (Rockwell mission 3 heating).

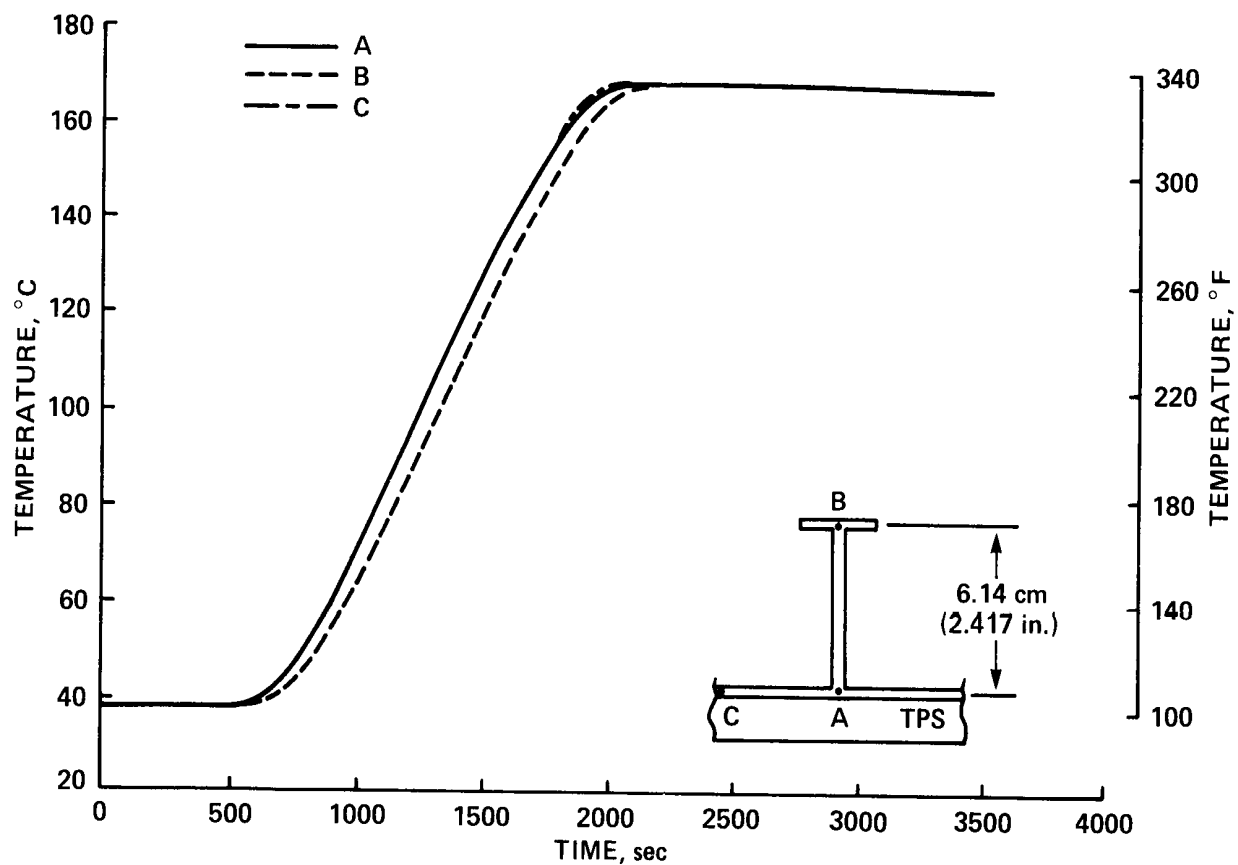


Figure 9. Temperature time histories at points in typical FS877 T-stiffener (no internal radiation).

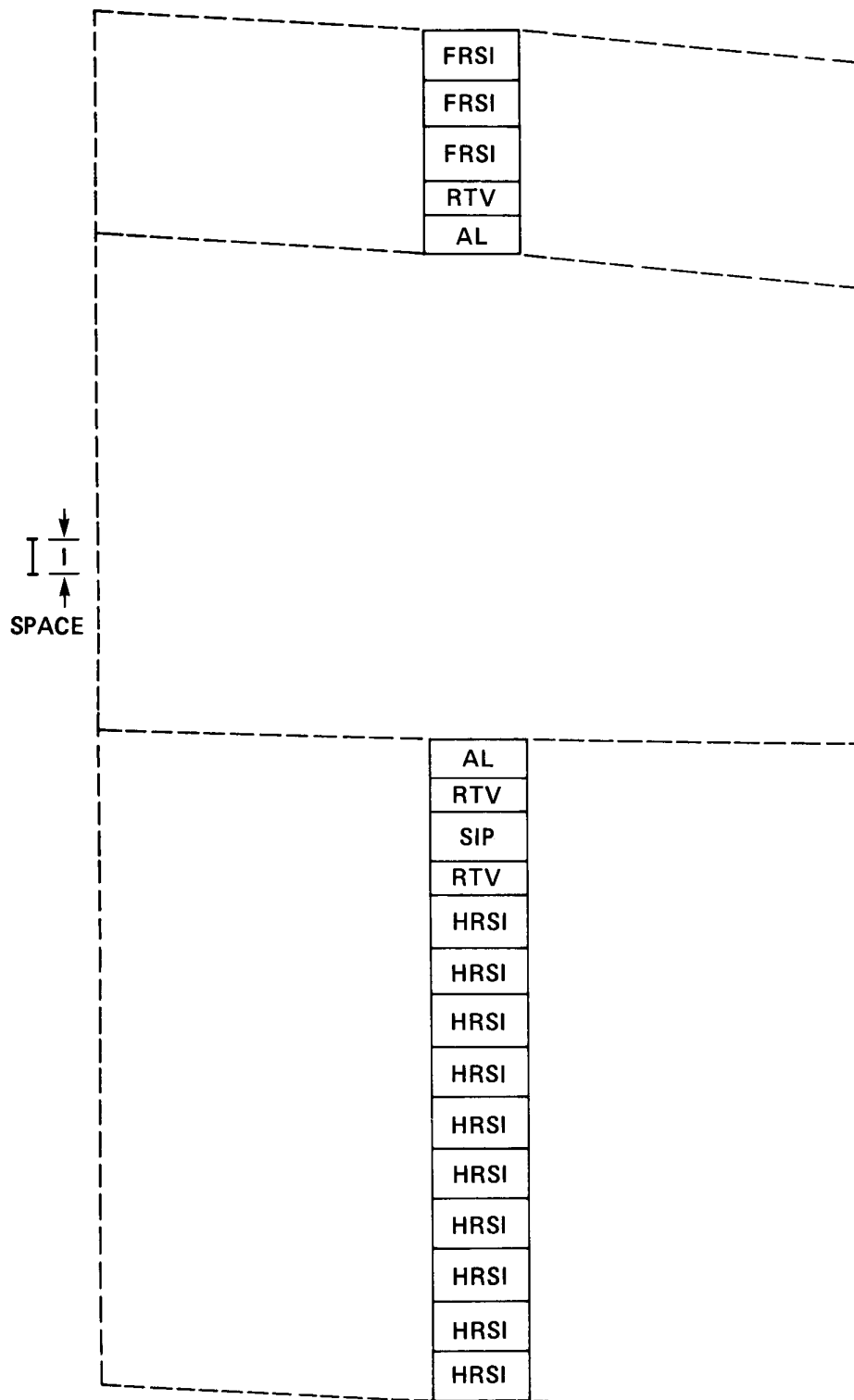


Figure 10. One-dimensional SPAR finite-element thermal model for WS240 bay 3 (number of JLOCs is 43).

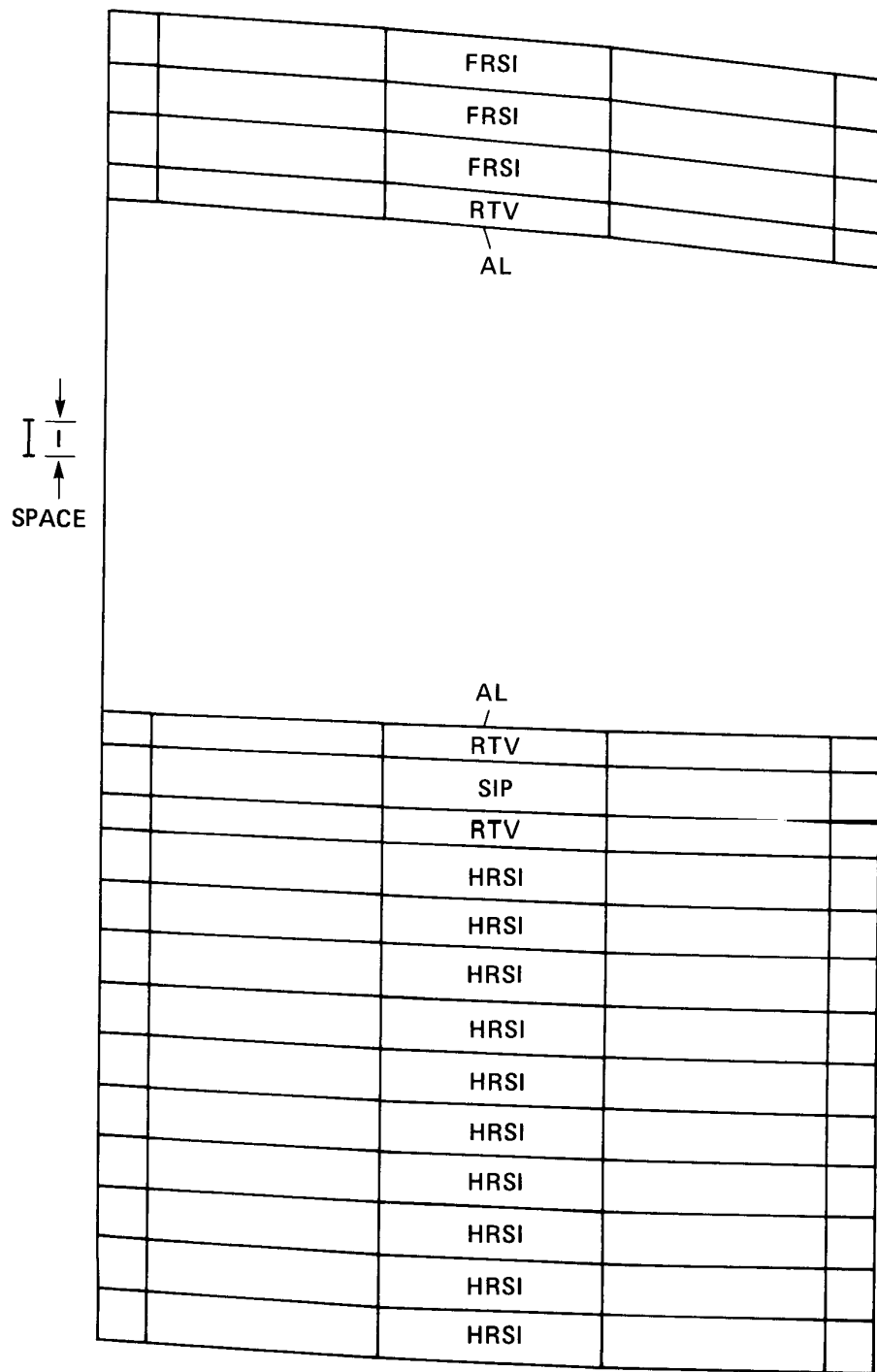


Figure 11. Two-dimensional SPAR finite-element thermal model for WS240 bay 3 (number of JLOCs is 123).

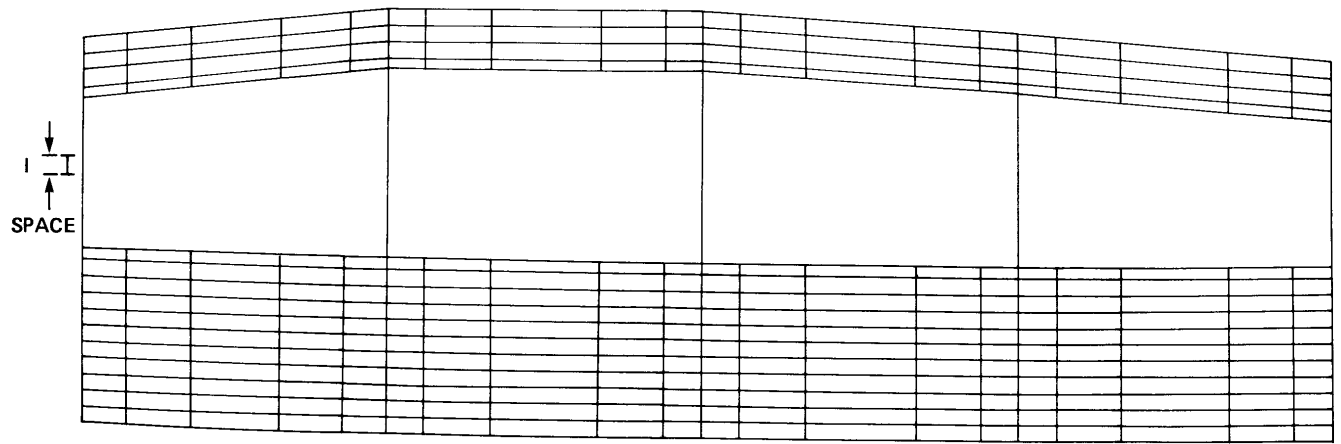


Figure 12. Two-dimensional SPAR finite-element thermal model for WS240 bay 3 (number of JLOCs is 383).

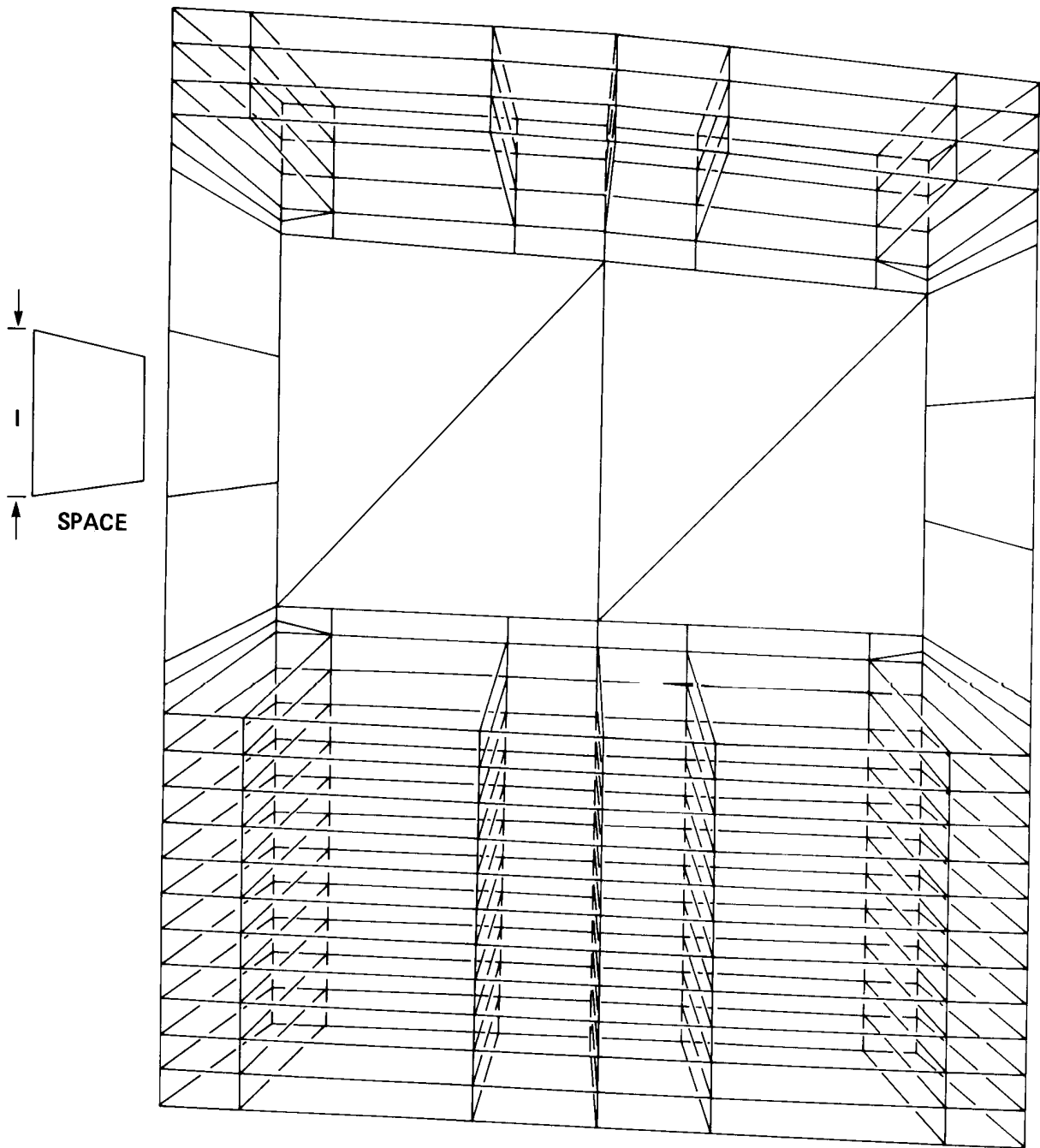


Figure 13. Three-dimensional SPAR finite-element thermal model for WS240 bay 3 (number of JLOCs is 268).

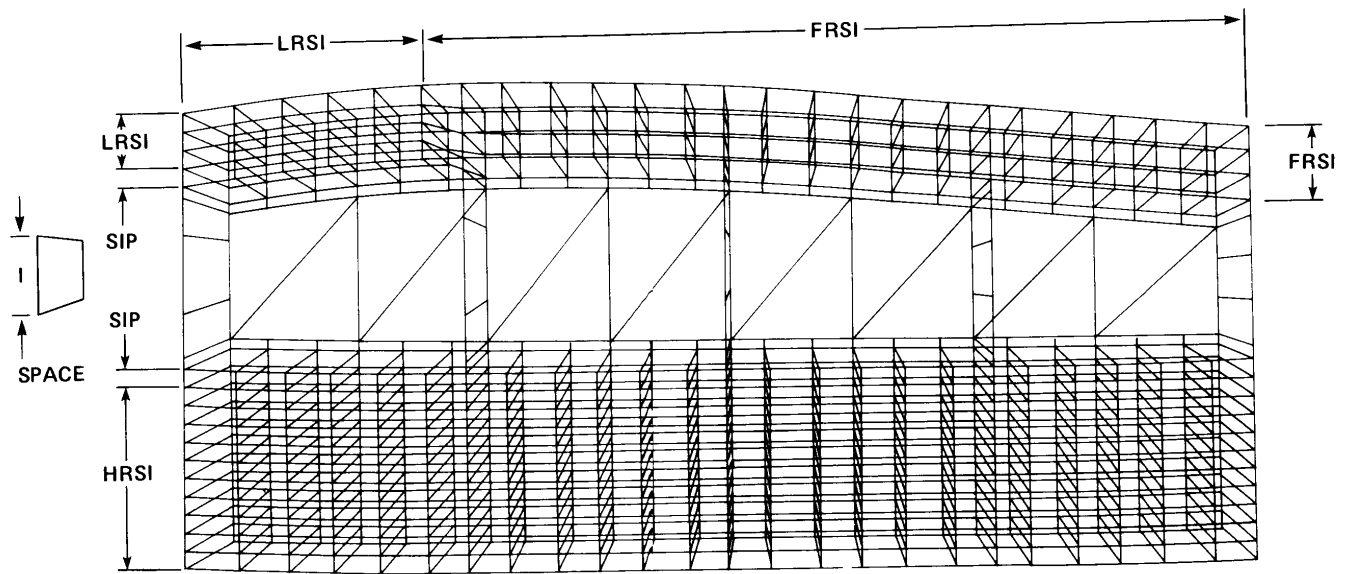


Figure 14. Three-dimensional SPAR finite-element thermal model for WS240 (number of JLOCs is 920).

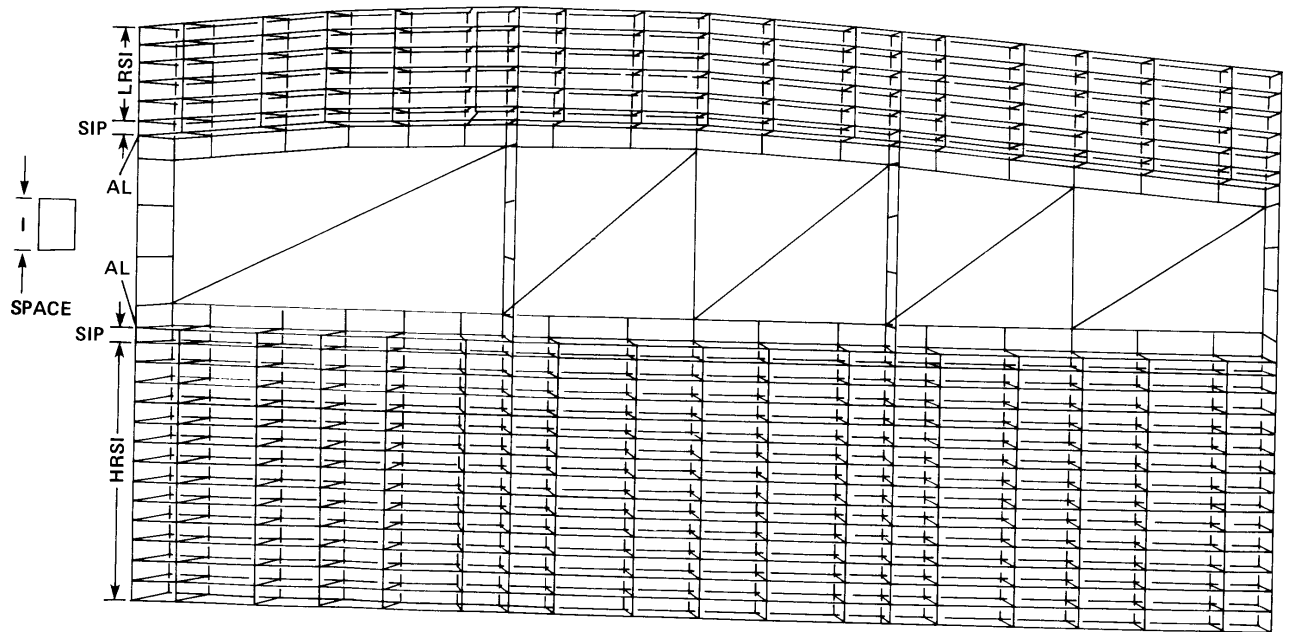


Figure 15. Three-dimensional SPAR finite-element thermal model for WS328 (number of JLOCs is 916).

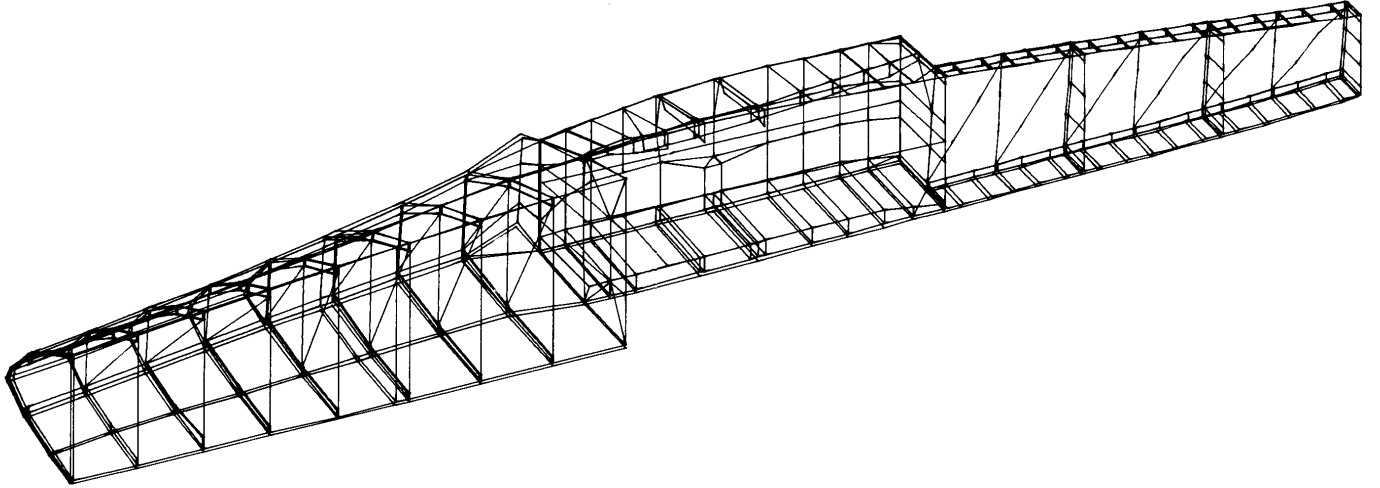


Figure 16. SPAR thermal model for WS134 (number of JLOCs is 2075).

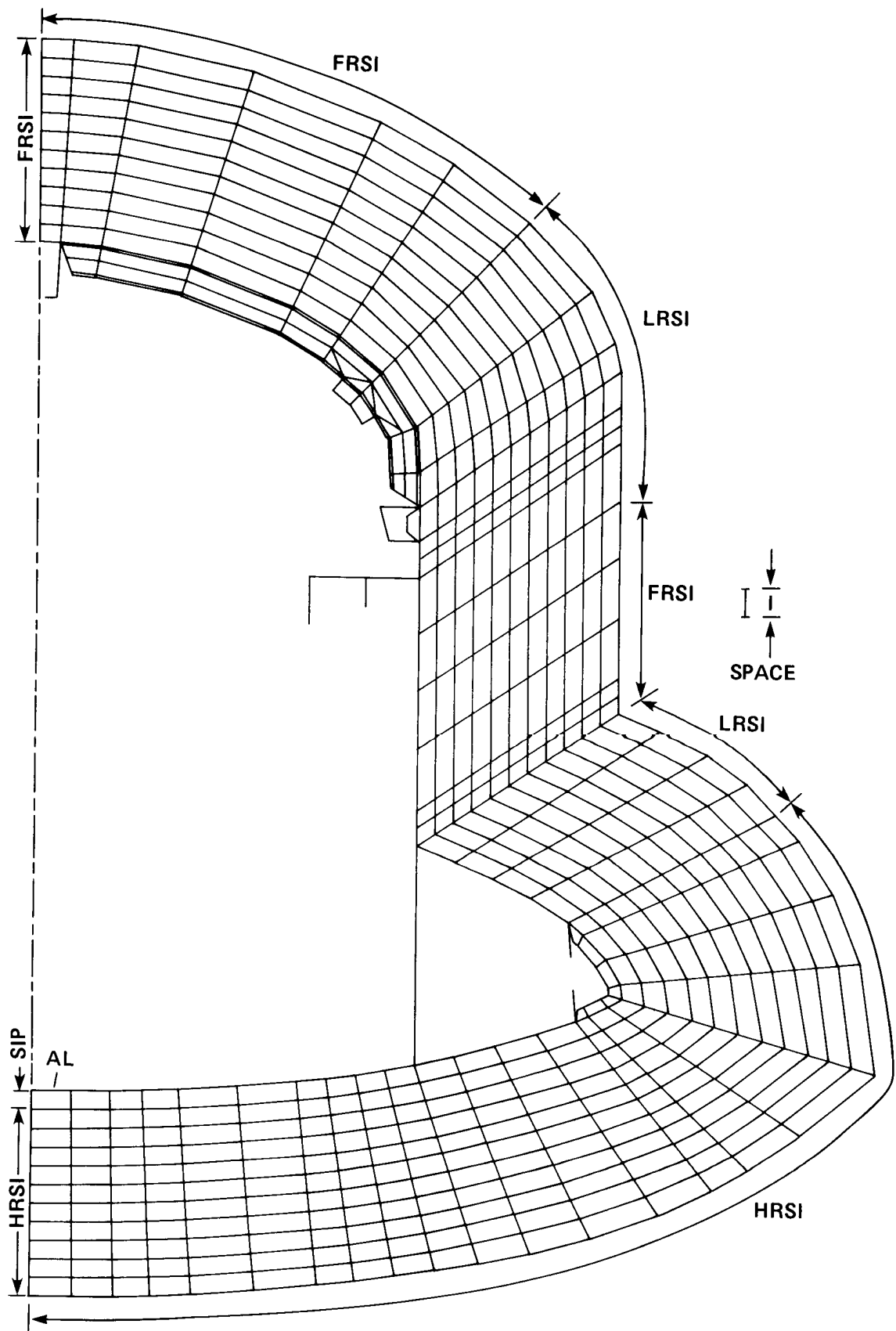


Figure 17. Two-dimensional SPAR finite-element thermal model for FS877 (number of JLOCs is 605).

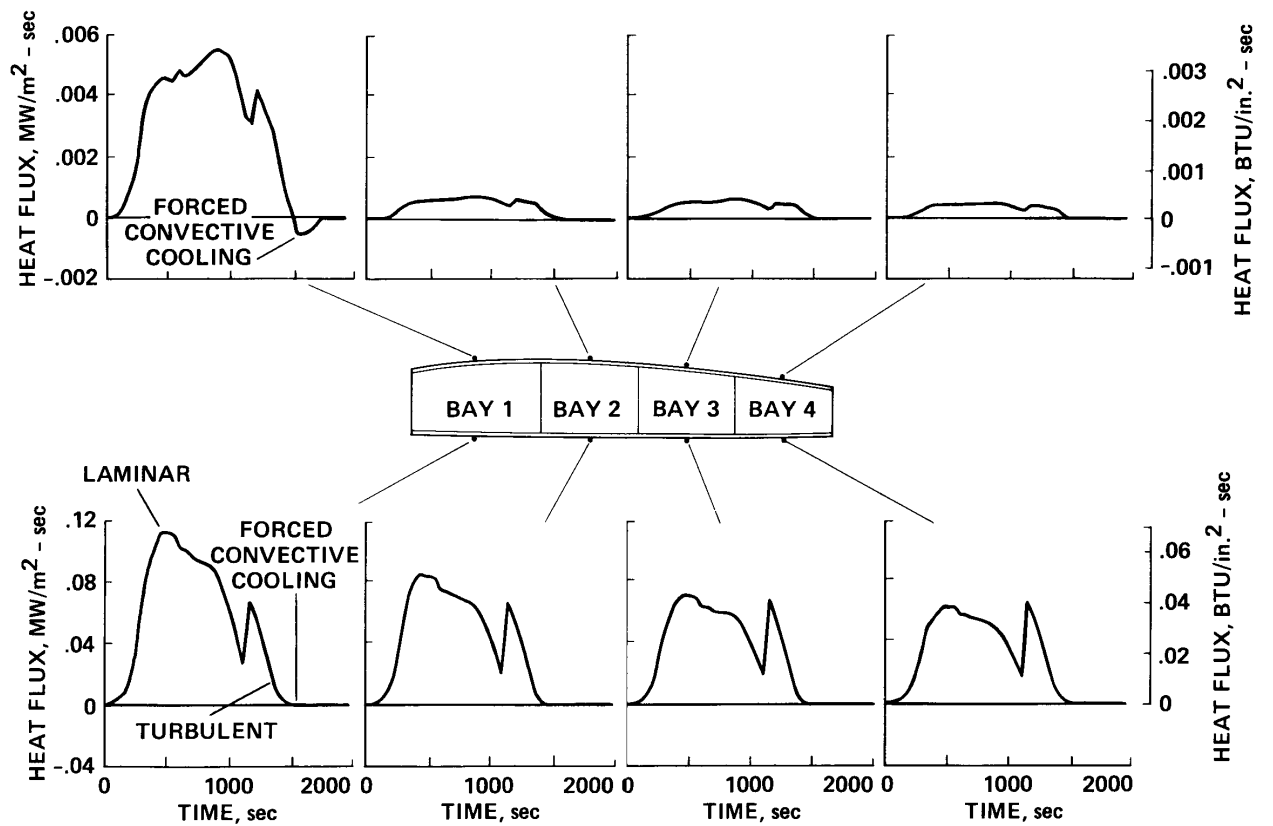


Figure 18. Surface heating rates at WS240 calculated for STS-5 flight.

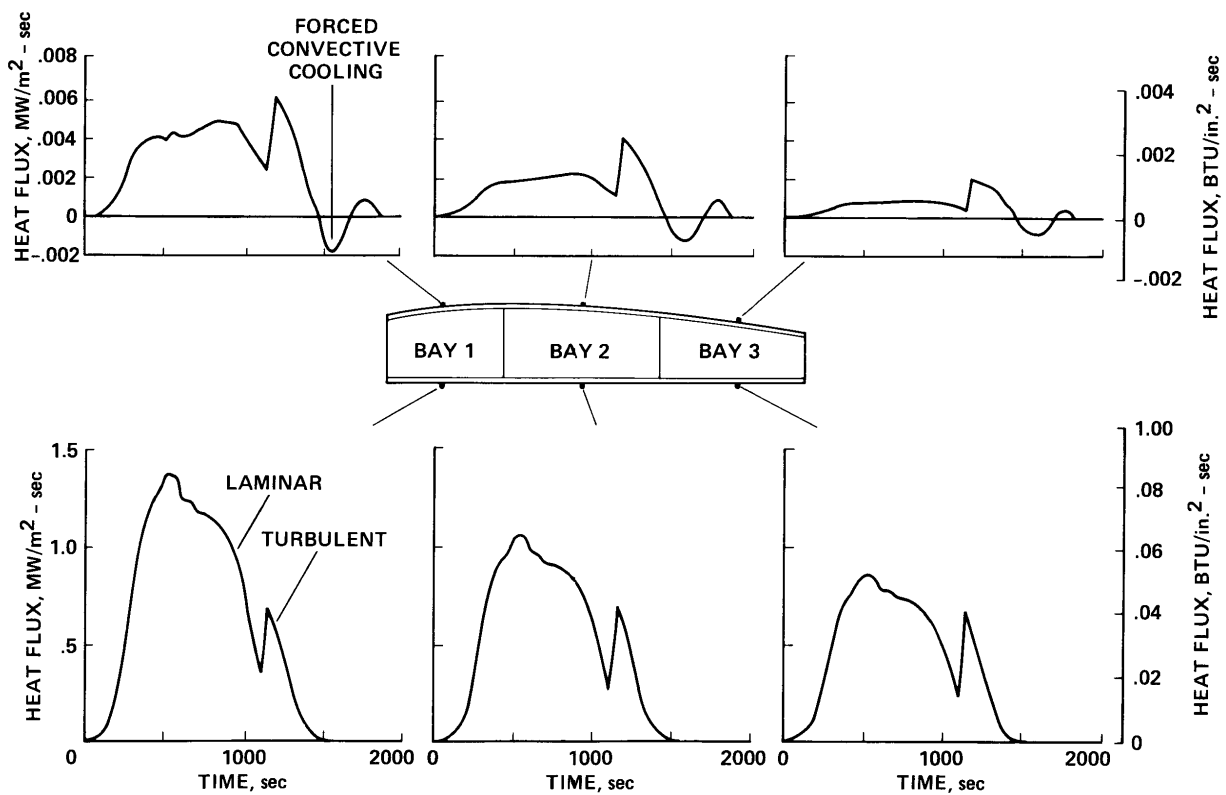


Figure 19. Surface heating rates at WS328 calculated for STS-5 flight.

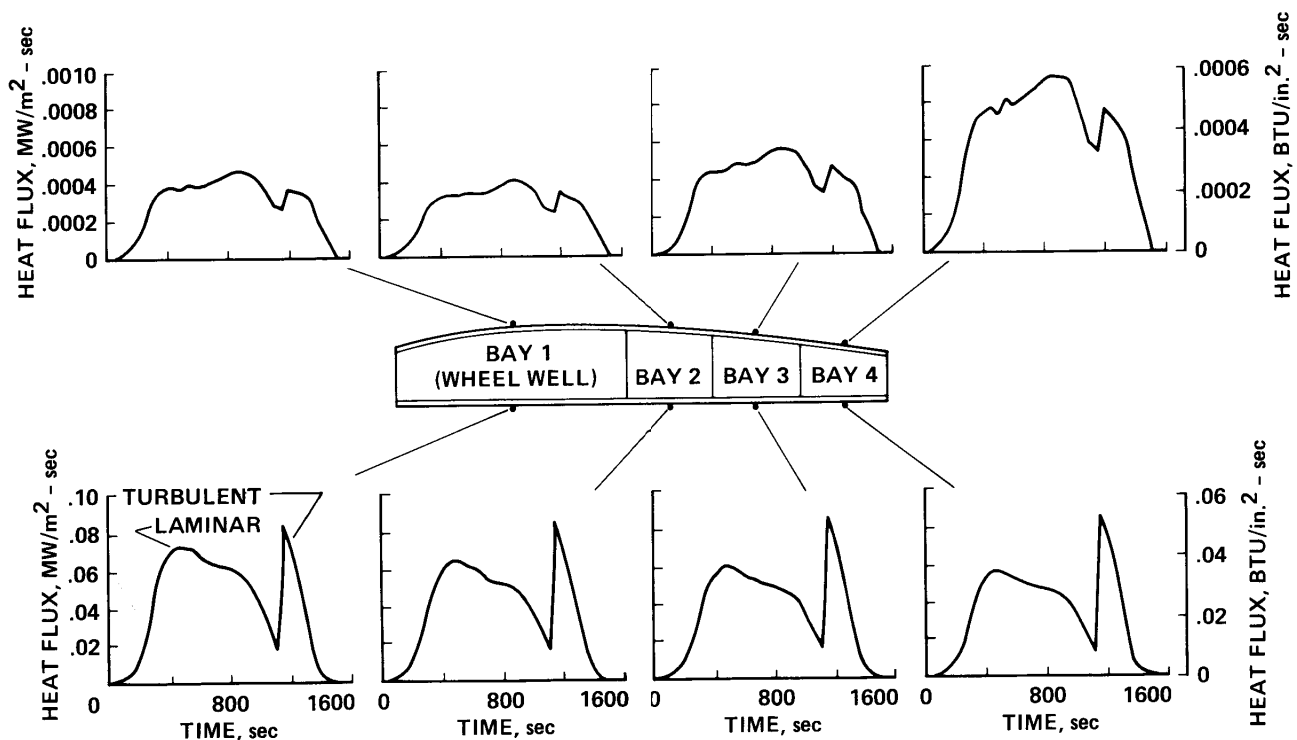


Figure 20. Surface heating rates at WS134 calculated for STS-5 flight.

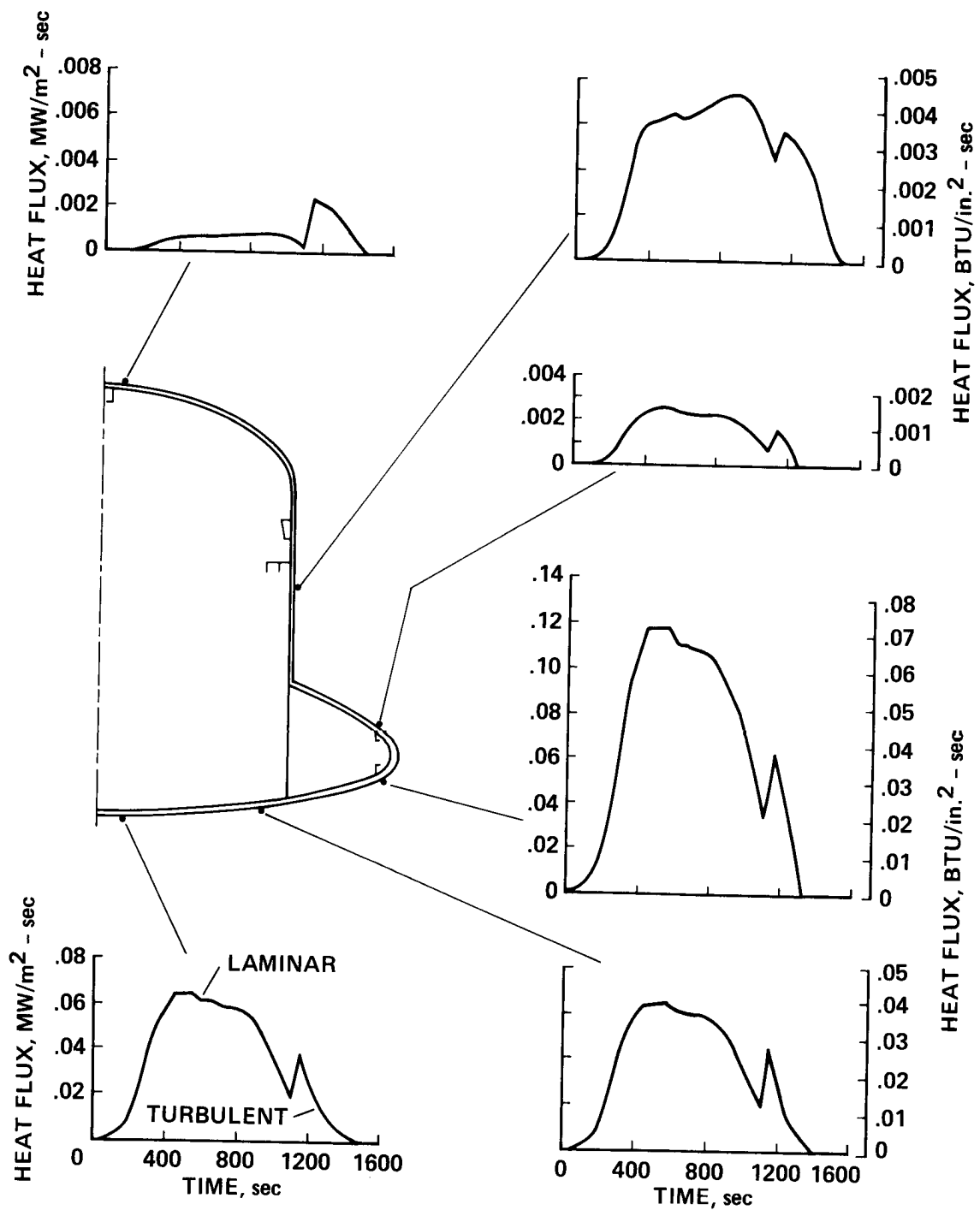


Figure 21. Surface heating rates at FS877 calculated for STS-5 flight.

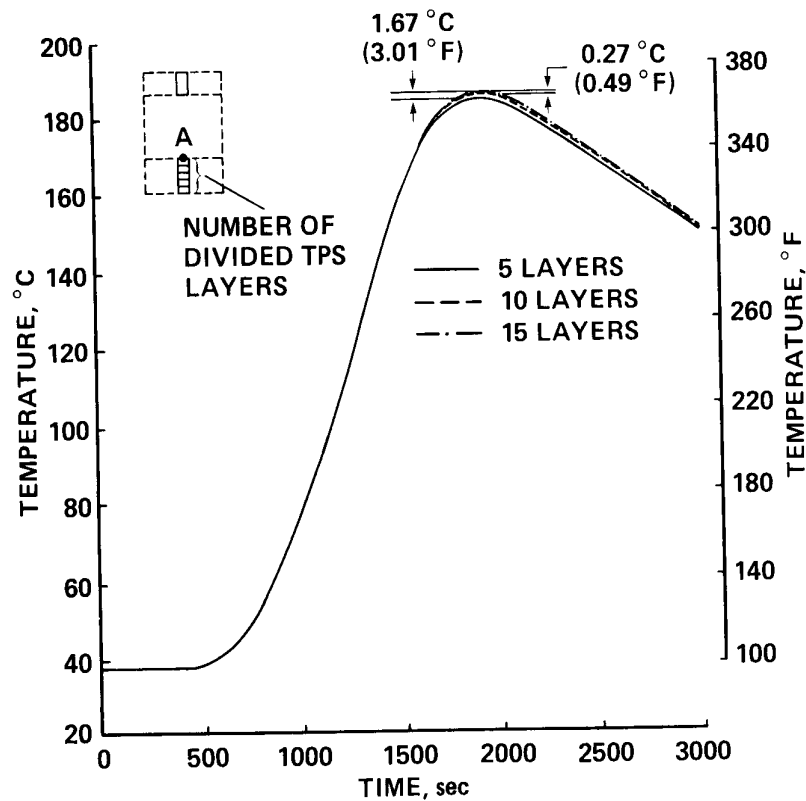


Figure 22. Effect of number of TPS layers on lower skin temperatures (WS240 bay 3 one-dimensional model, Rockwell mission 3 heating).

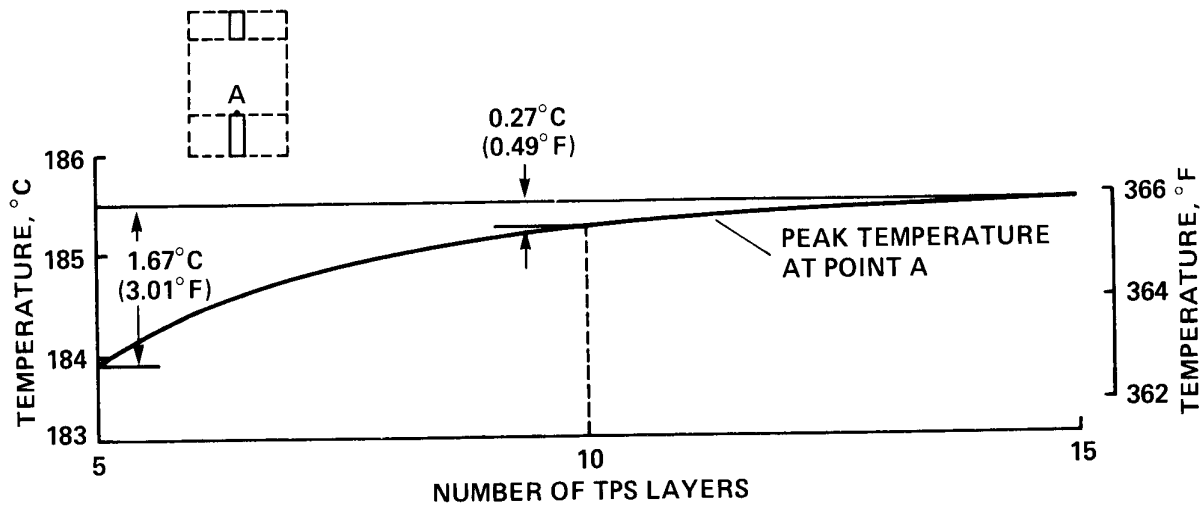


Figure 23. Variation of peak lower skin temperatures with number of TPS layers (WS240 bay 3 one-dimensional model, Rockwell mission 3 heating).

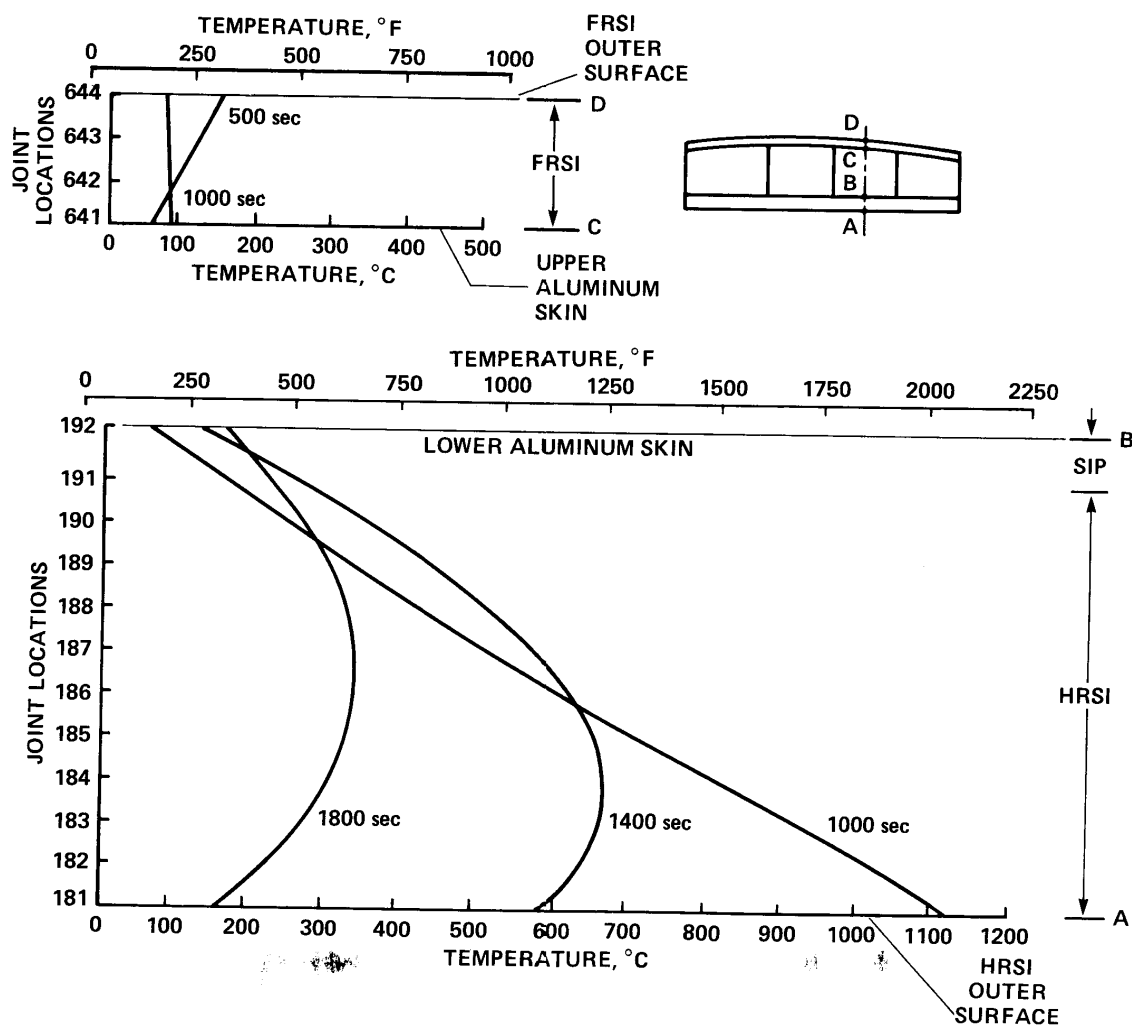


Figure 24. Temperature distributions in HRSI and FRSI for WS240 bay 3 SPAR three-dimensional model (Rockwell mission 3 heating).

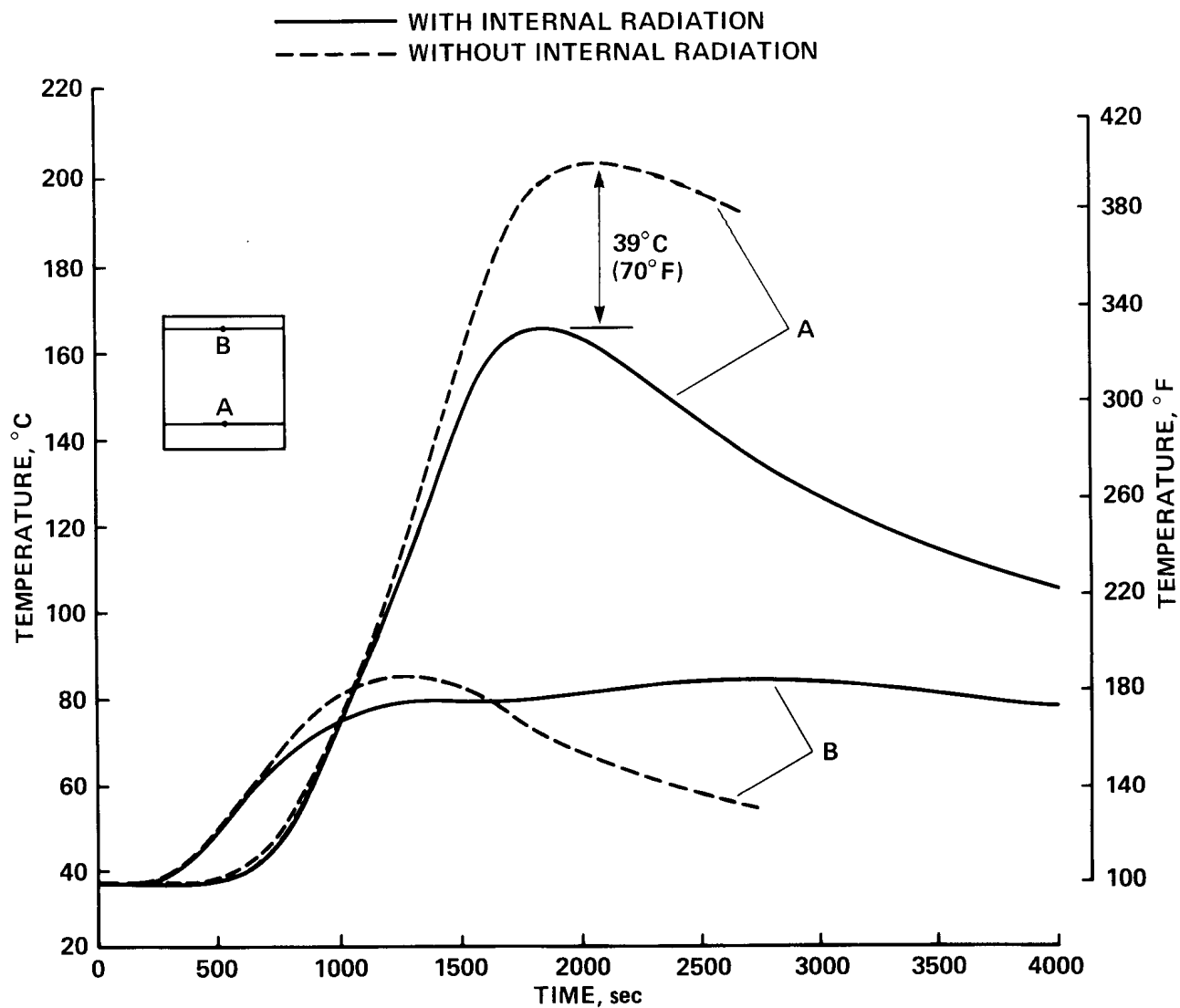


Figure 25. Effect of internal radiation on lower and upper skin temperatures on three-dimensional one-cell model for WS240 bay 3 (Rockwell mission 3 heating).

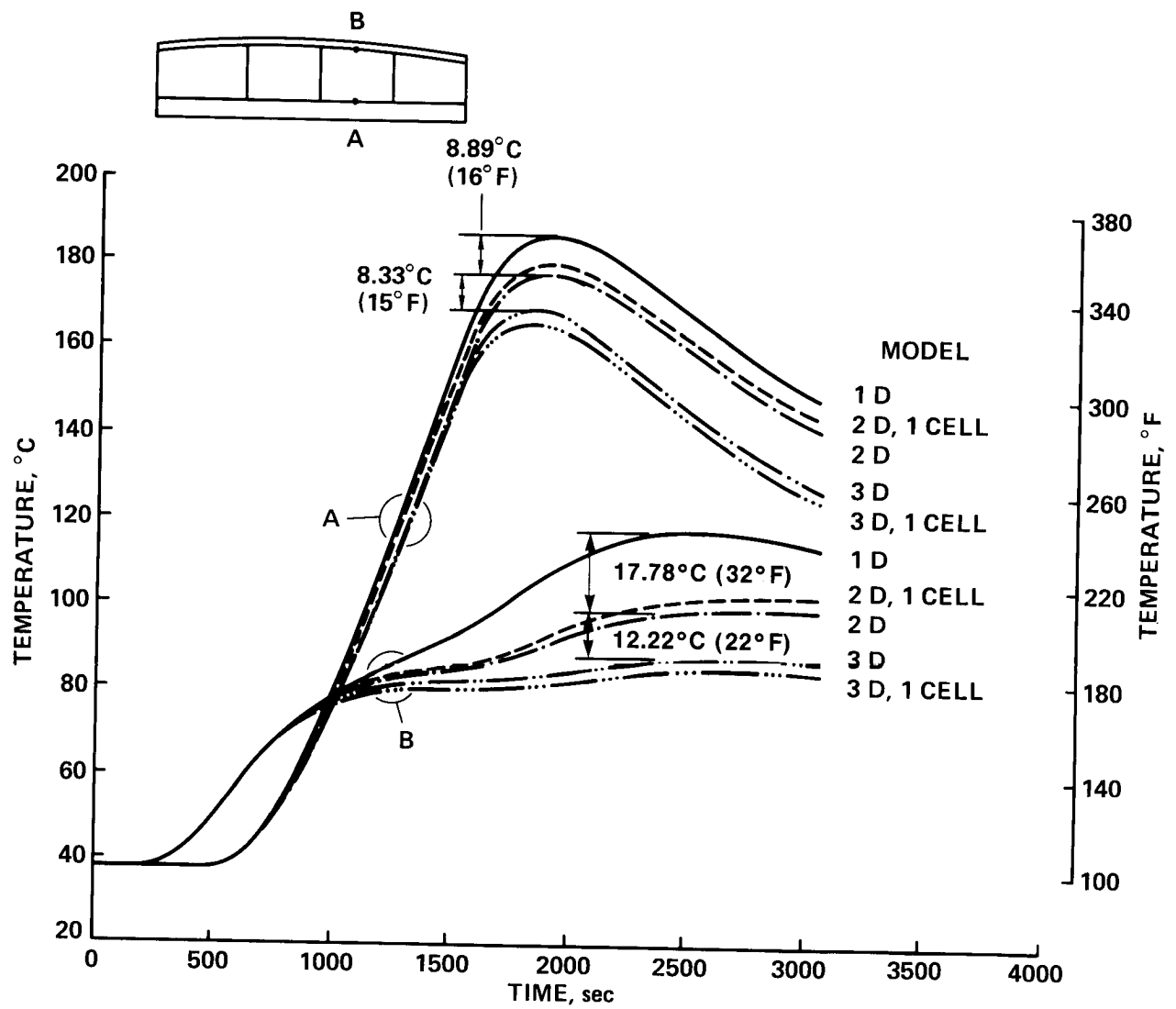


Figure 26. Time histories of lower and upper skin temperatures for WS240 bay 3 based on different finite-element models (Rockwell mission 3 heating).

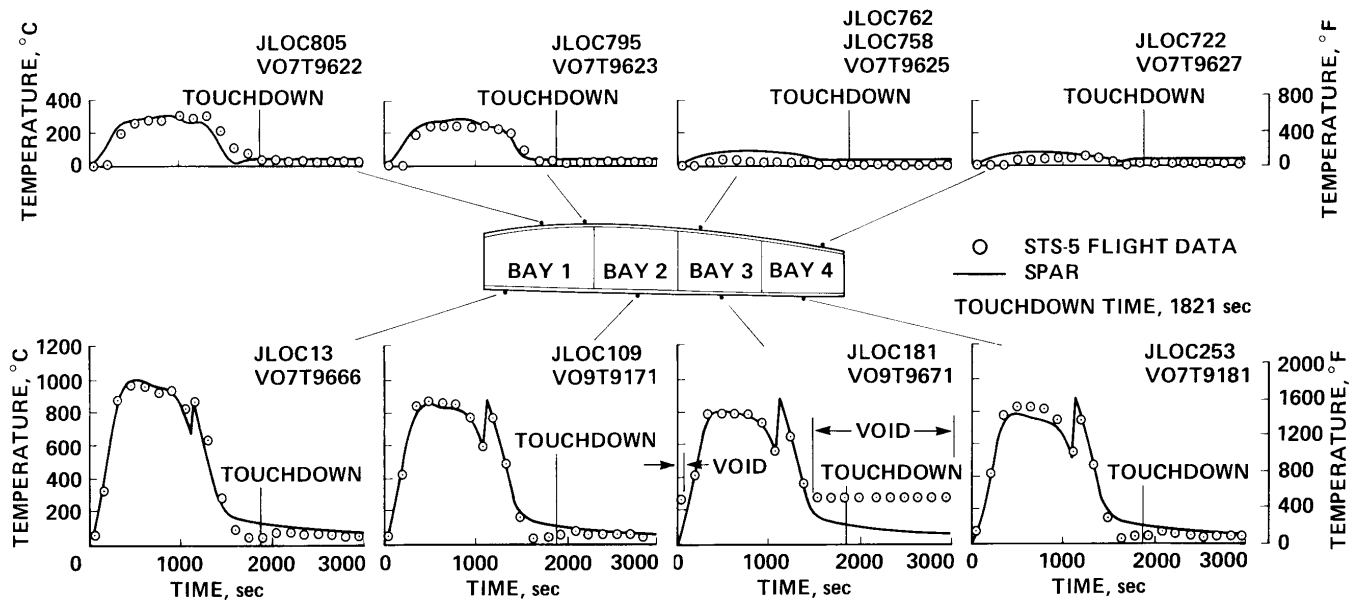


Figure 27. Time histories of TPS surface temperatures for WS240 (STS-5 flight).

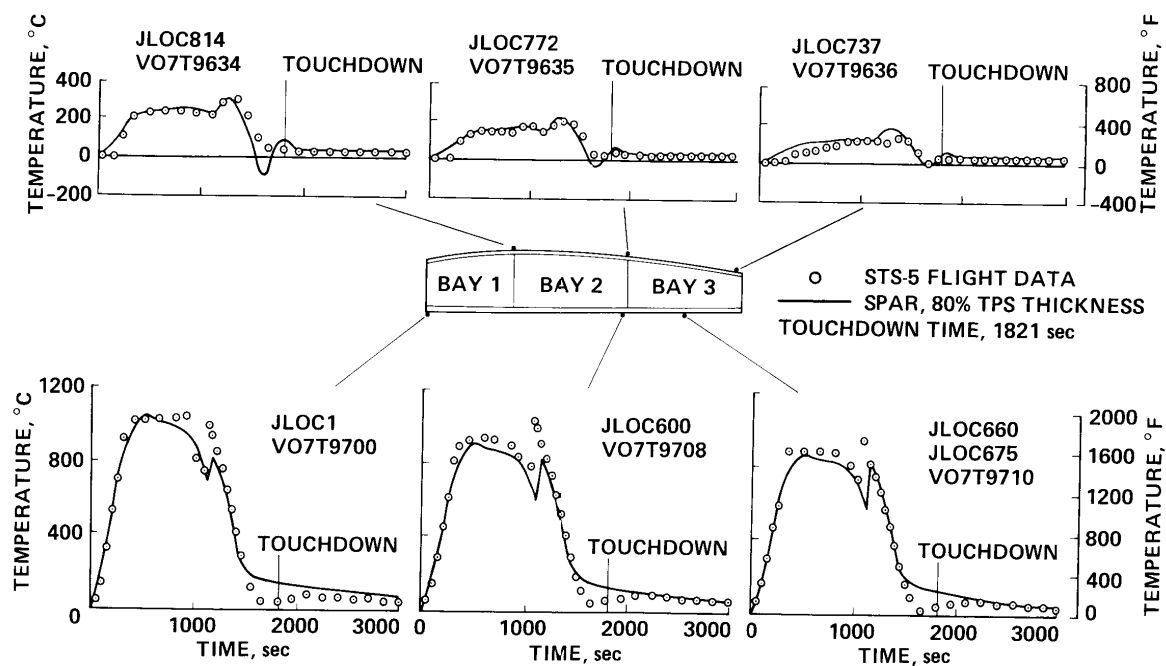


Figure 28. Time histories of TPS surface temperatures for WS328 (STS-5 flight).

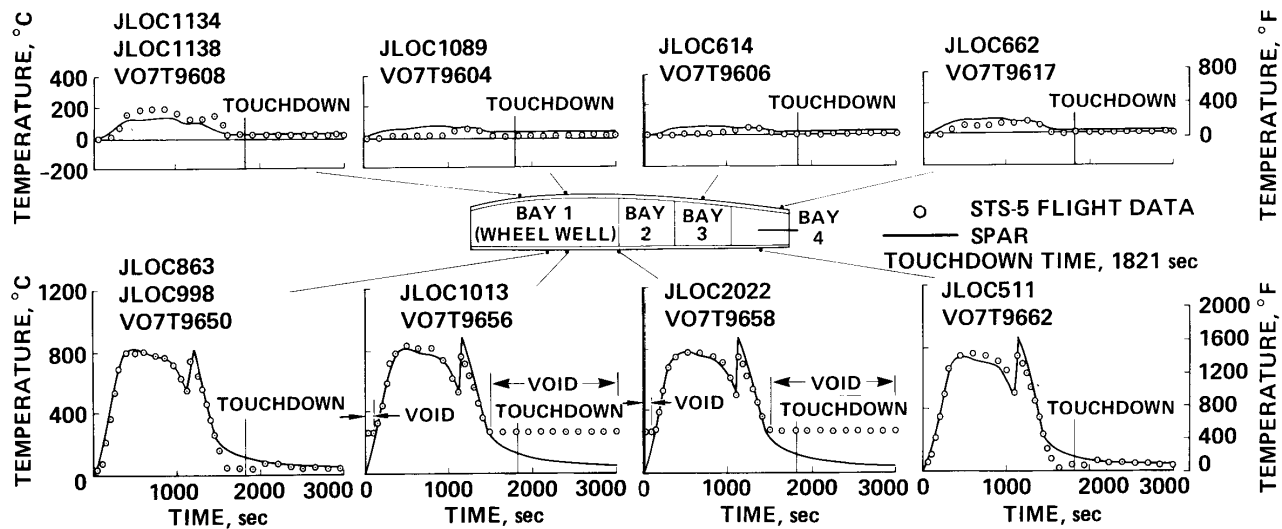


Figure 29. Time histories of TPS surface temperatures for WS134 (STS-5 flight).

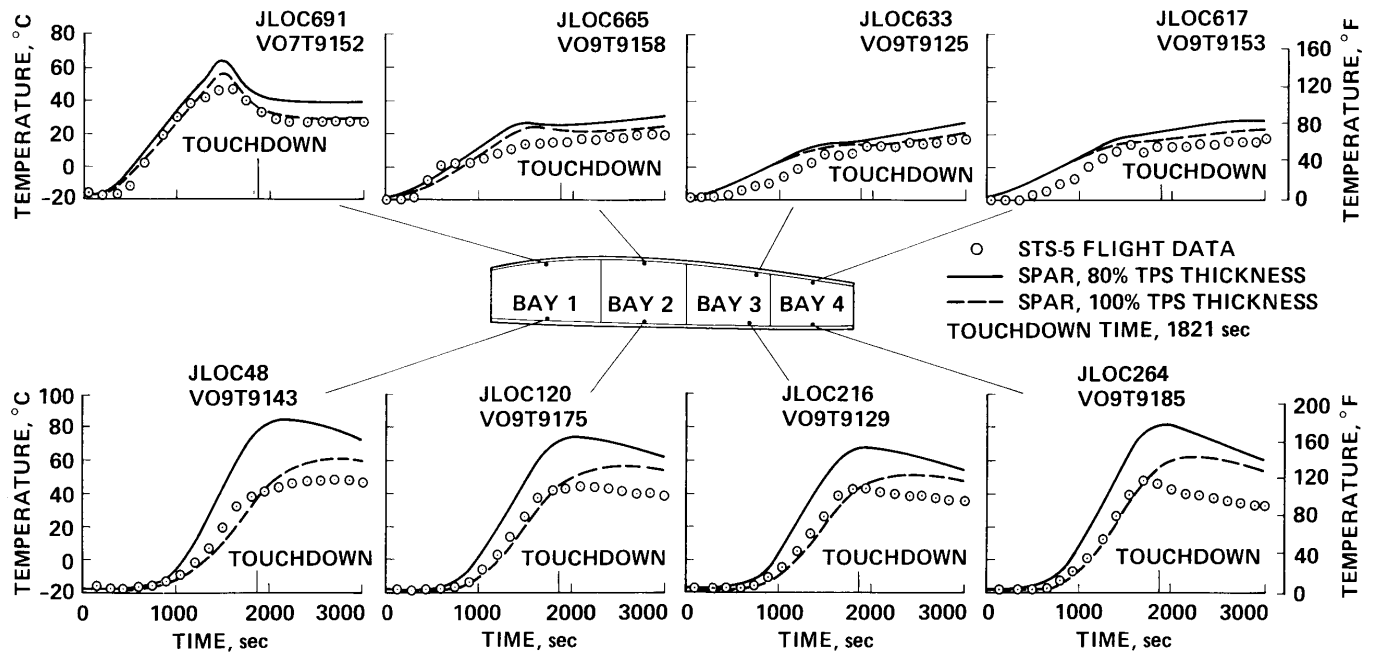


Figure 31. Time histories of structural temperatures for WS240 (STS-5 flight).

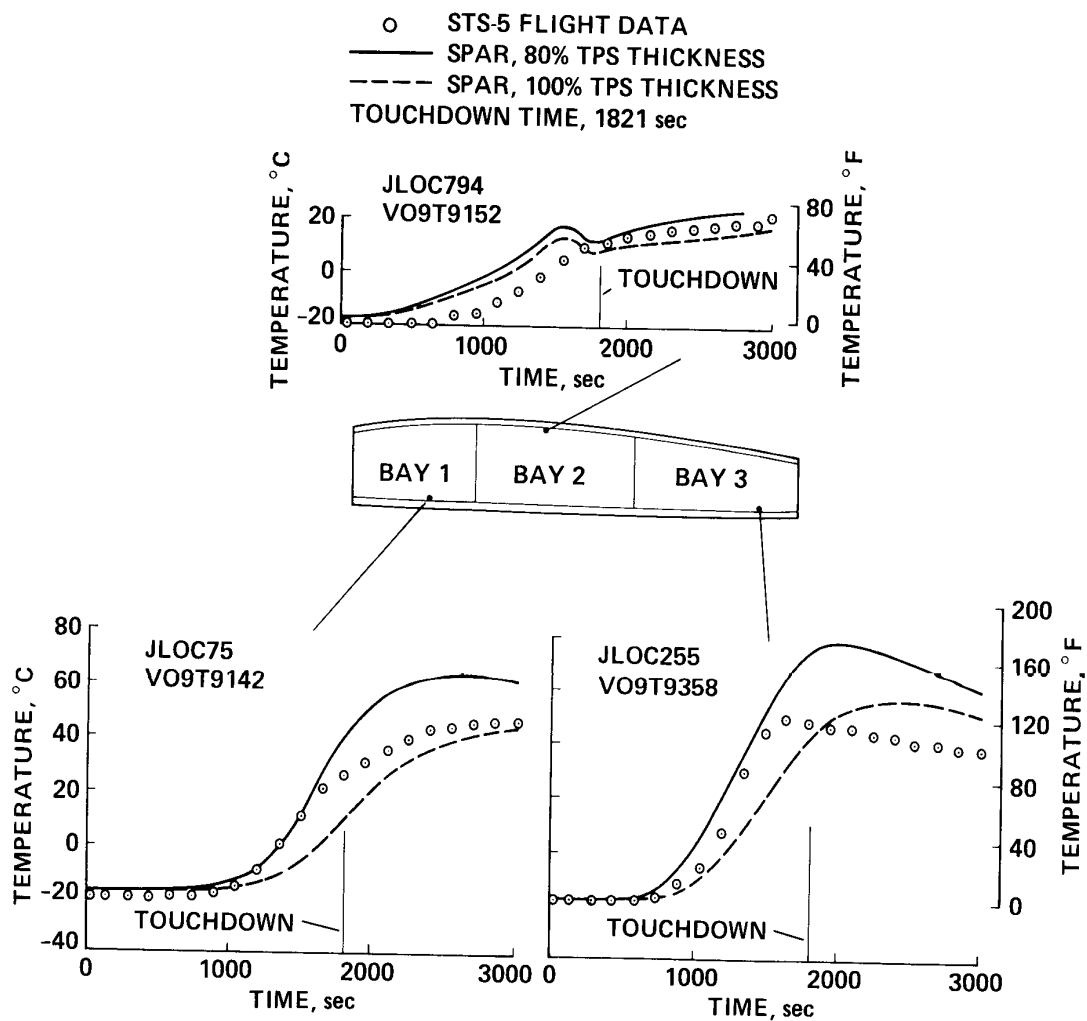


Figure 32. Time histories of structural temperatures for WS328 (STS-5 flight).

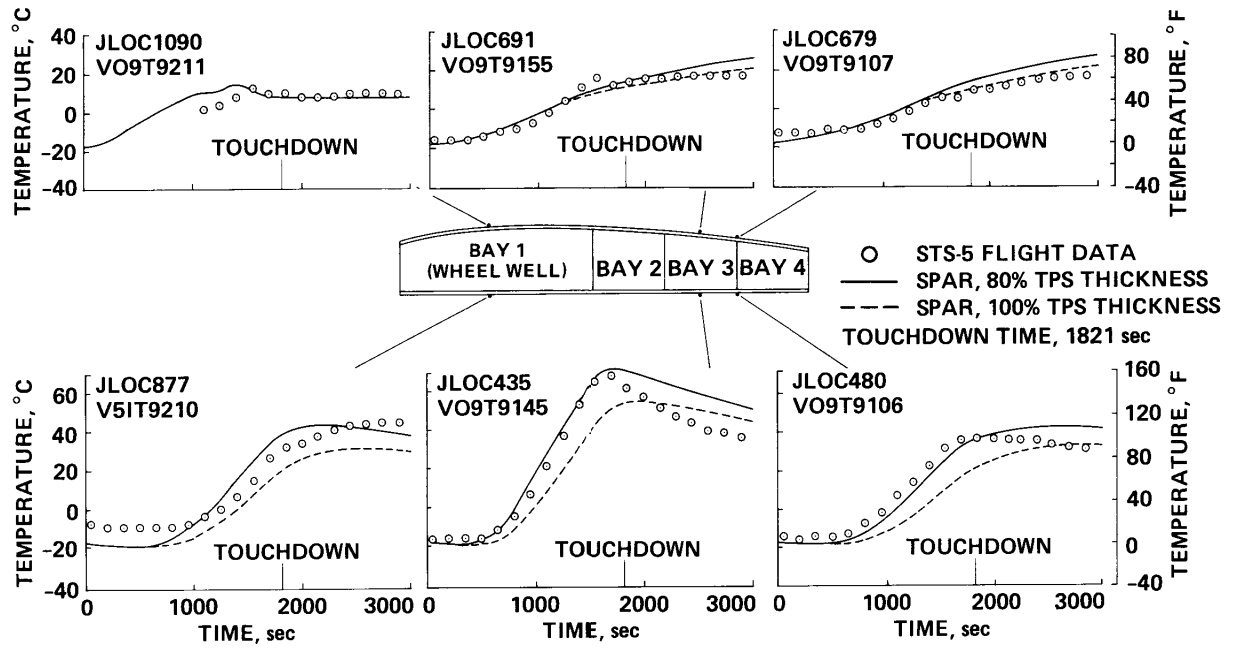


Figure 33. Time histories of structural temperatures for WS134 (STS-5 flight).

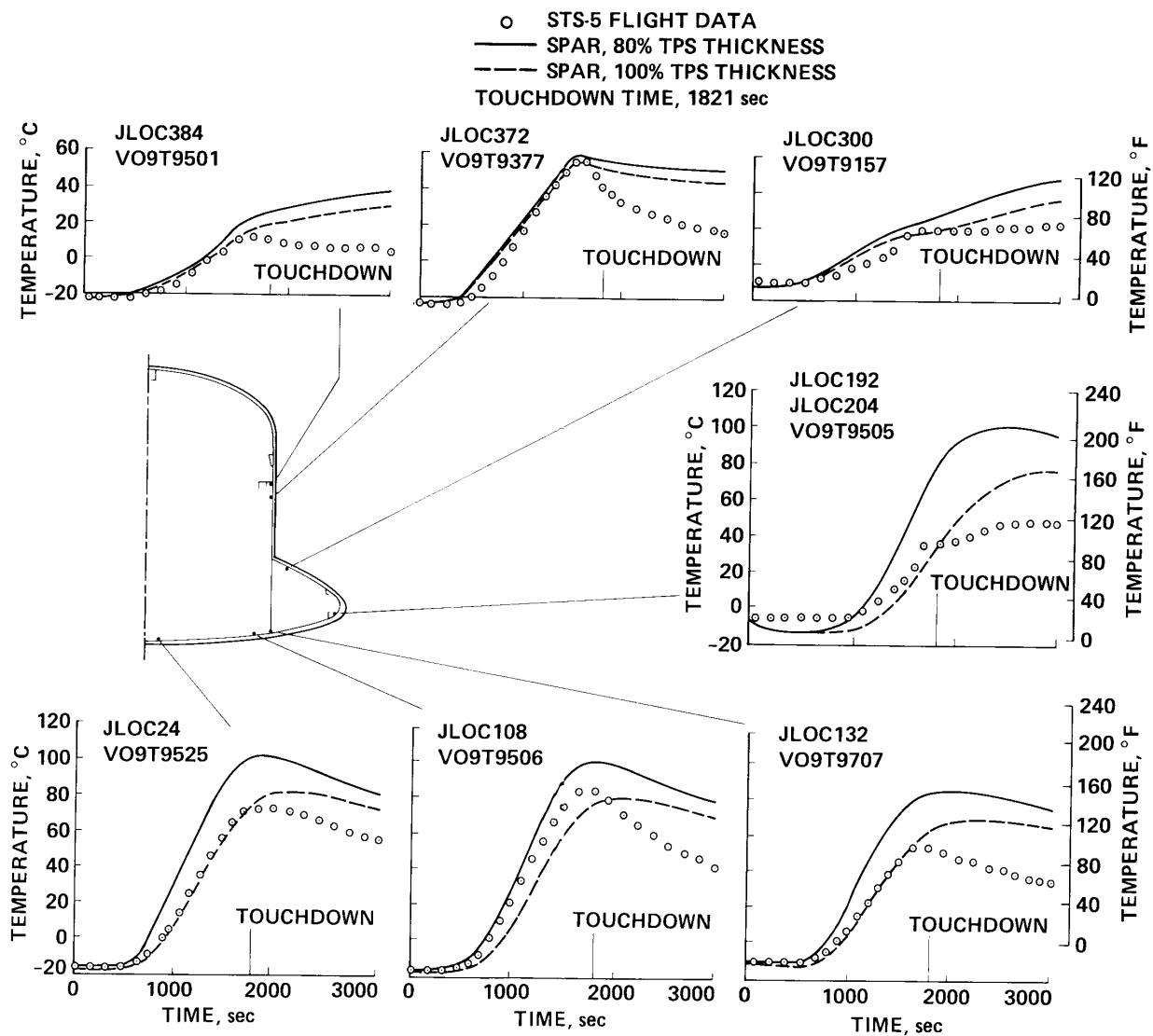


Figure 34. Time histories of structural temperatures for FS877 (STS-5 flight).

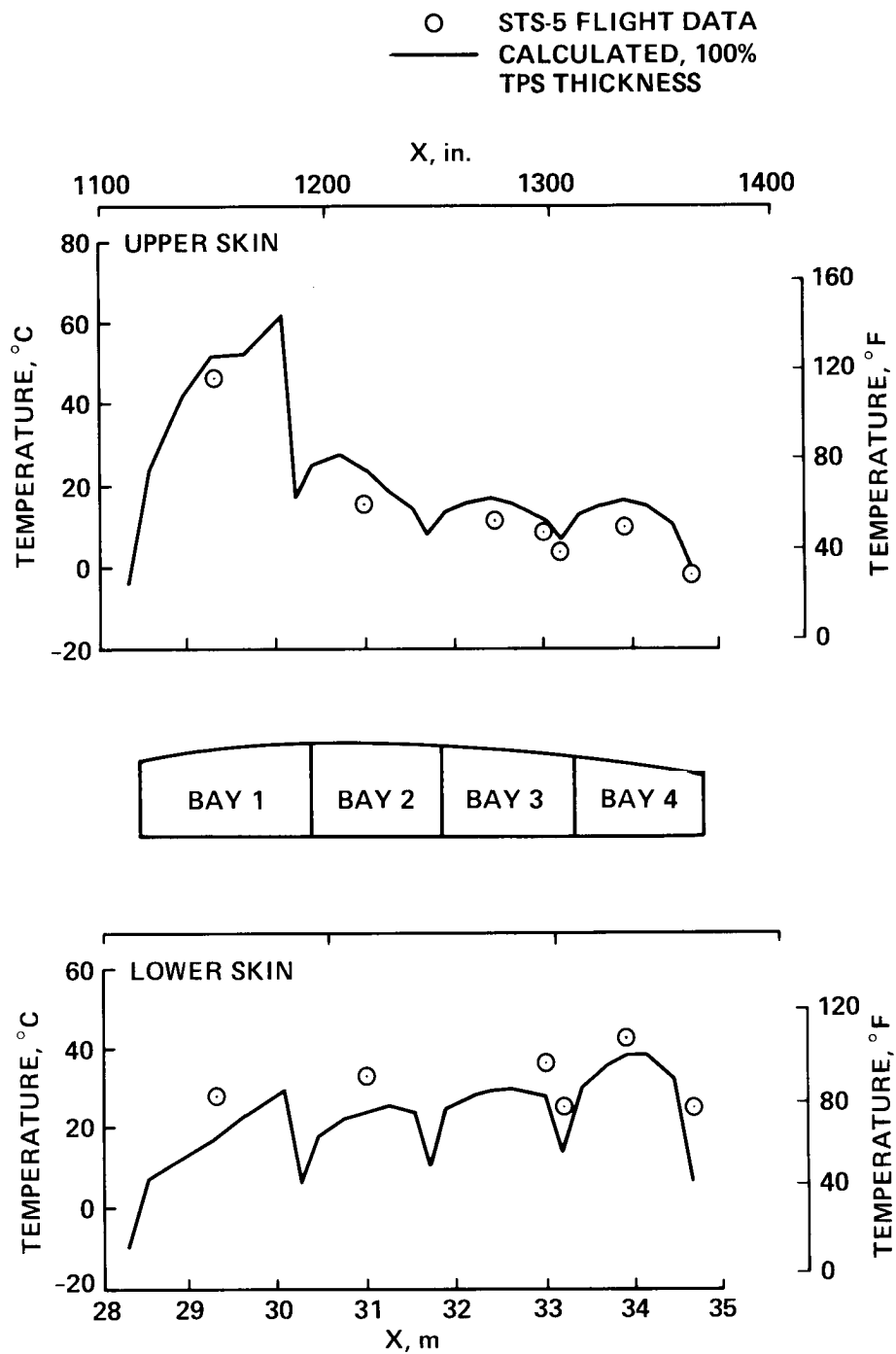


Figure 35. Chordwise distribution of aluminum skin temperatures for WS240 (STS-5 flight, $t = 1600$ sec).

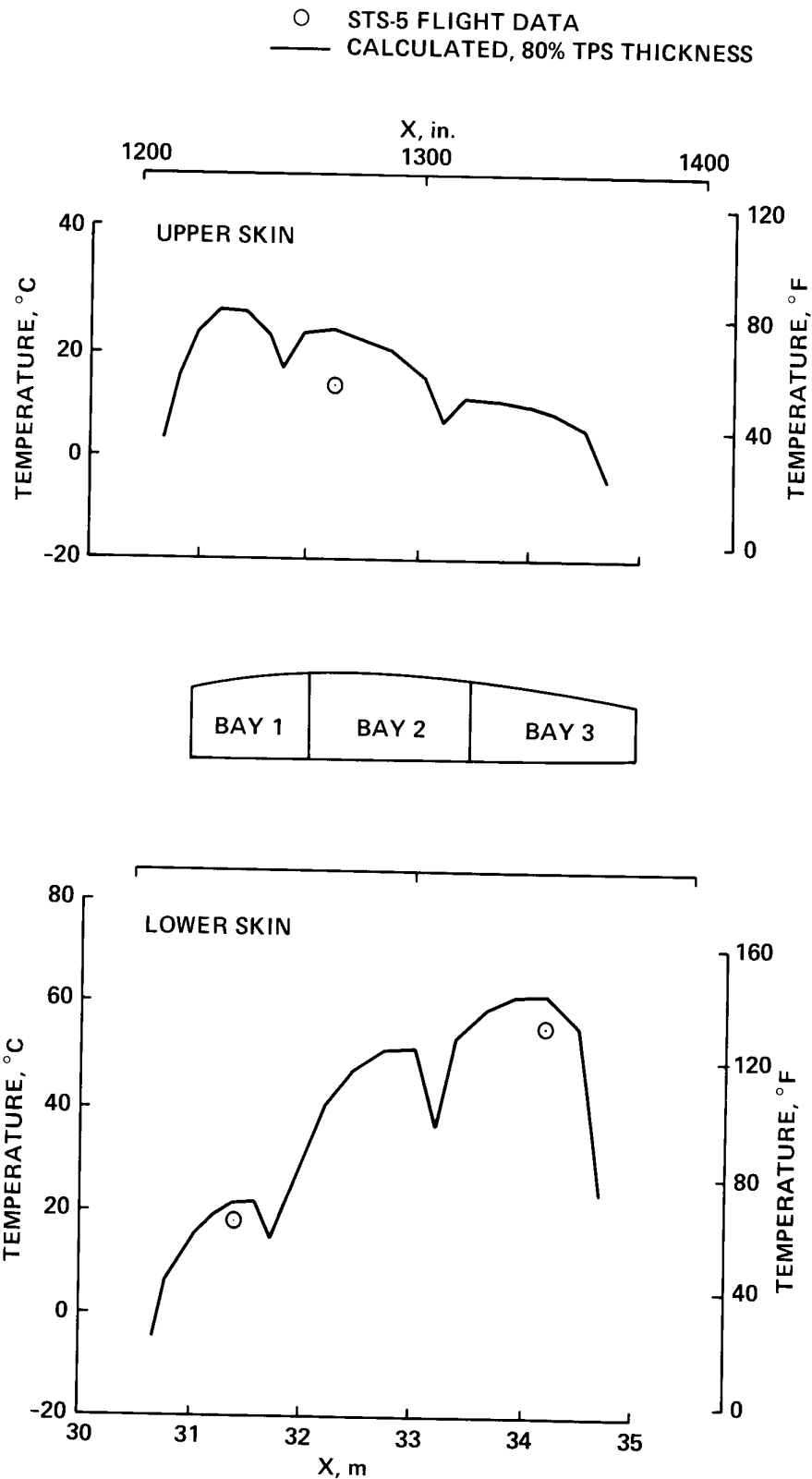


Figure 36. Chordwise distribution of aluminum skin temperatures for WS328 (STS-5 flight, $t = 1600$ sec).

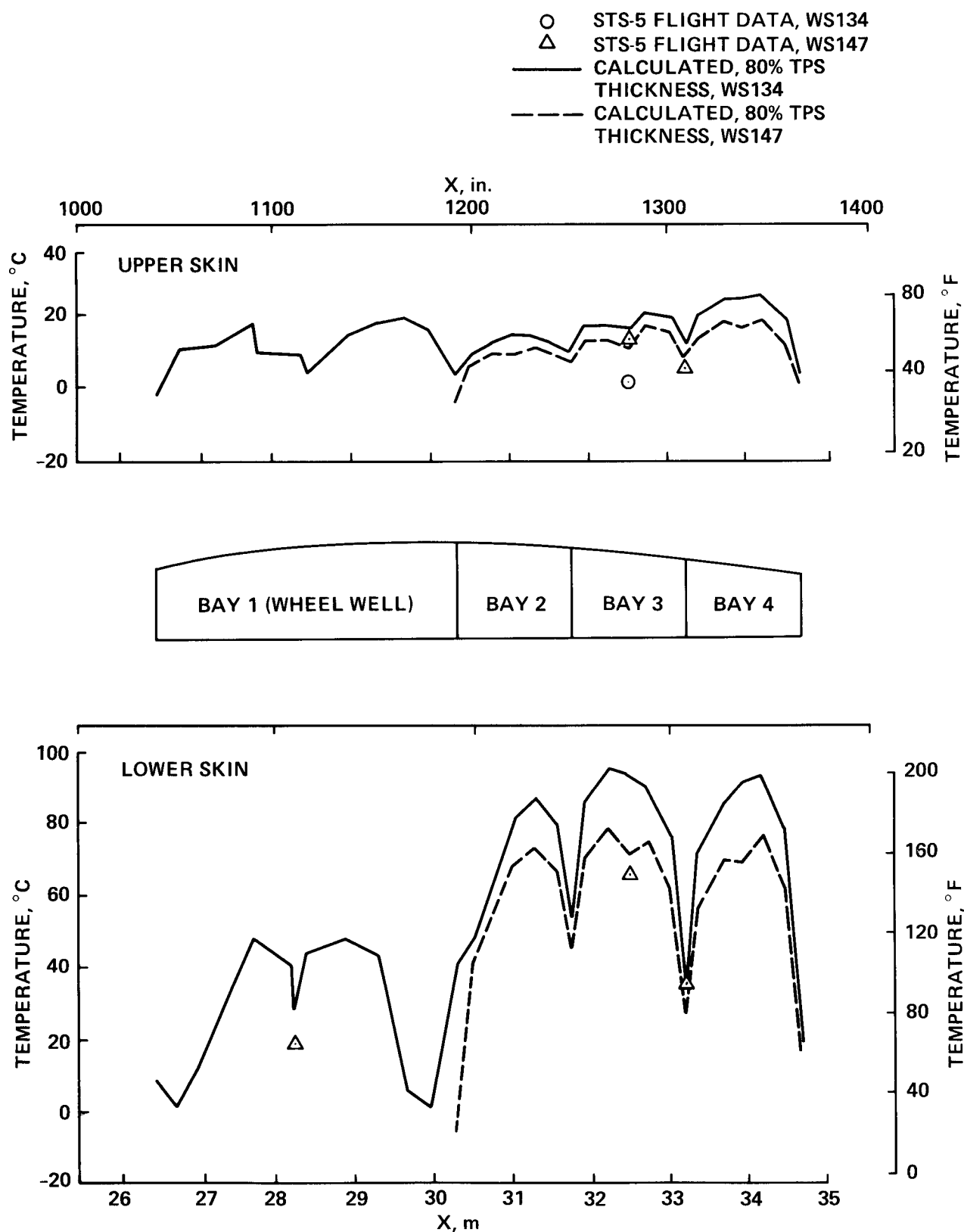


Figure 37. Chordwise distributions of aluminum skin temperatures for WS134 and WS147 (STS-5 flight, $t = 1600$ sec).

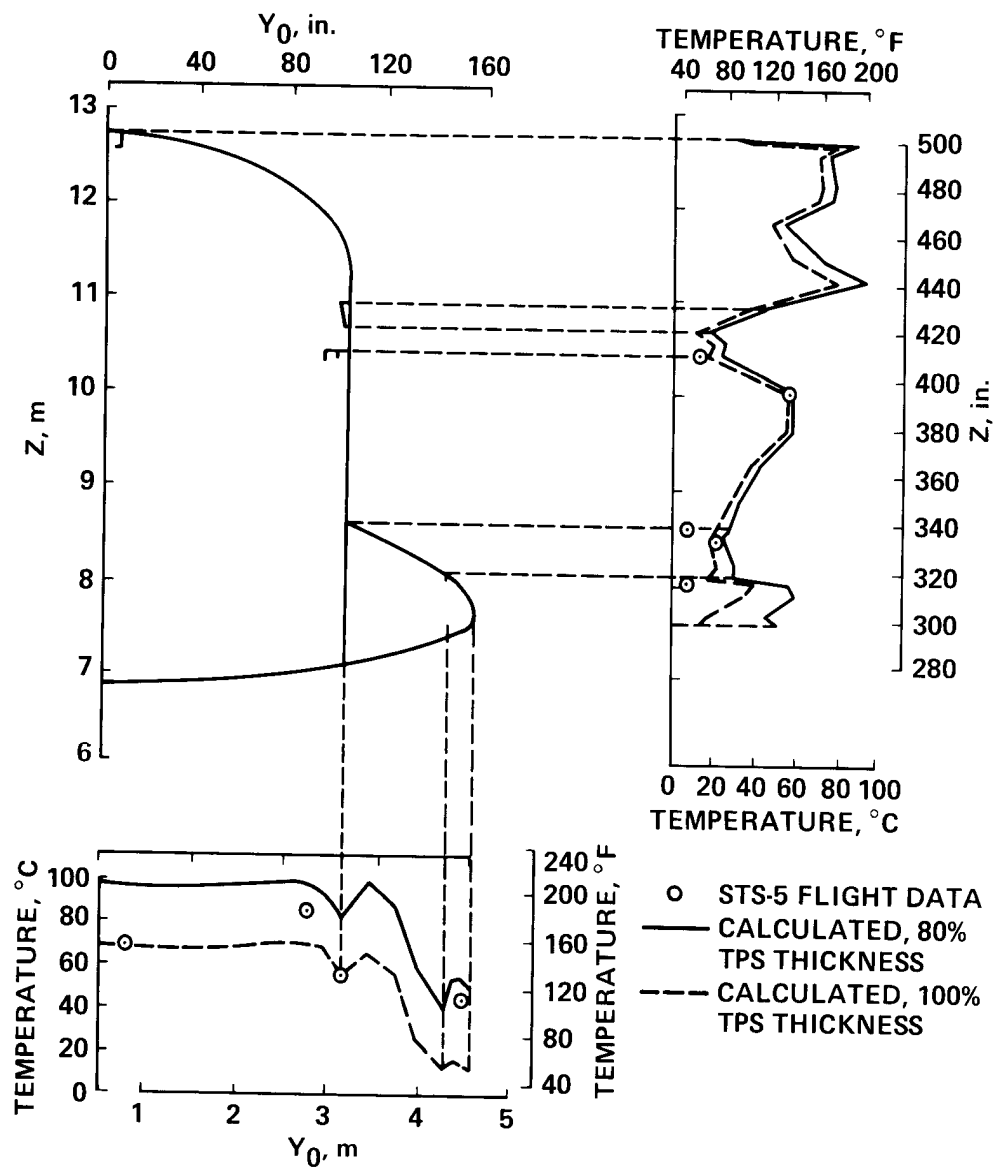


Figure 38. Circumferential distribution of structural temperatures for FS877 (STS-5 flight, $t = 1600$ sec).

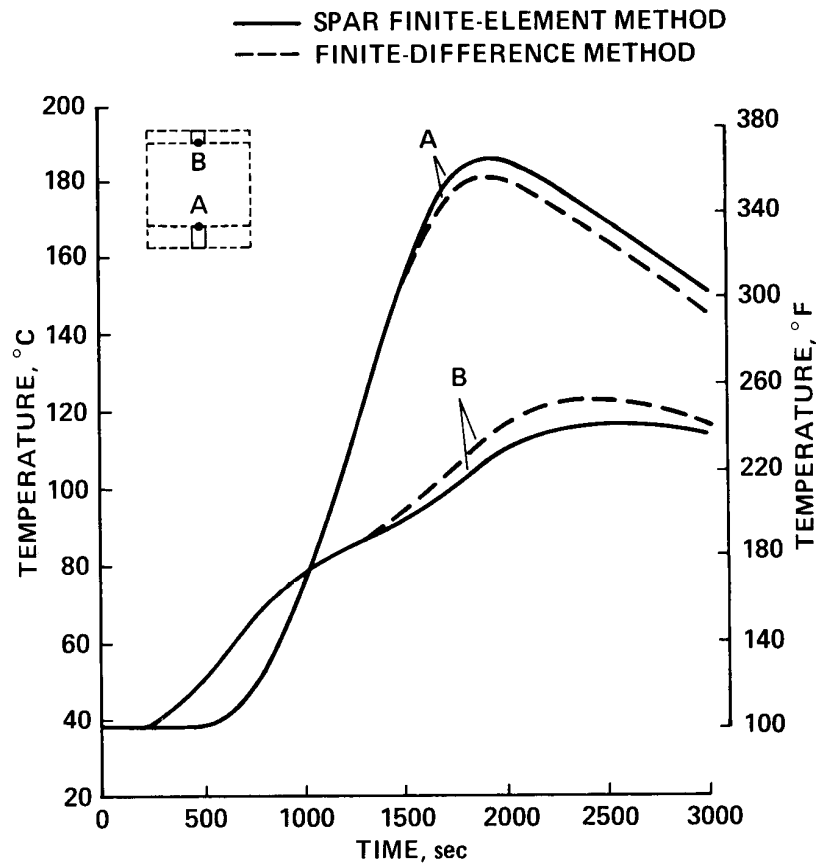


Figure 39. Comparison of WS240 bay 3 structural temperatures predicted by SPAR finite-element and finite-difference methods for one-dimensional model (Rockwell mission 3 heating).

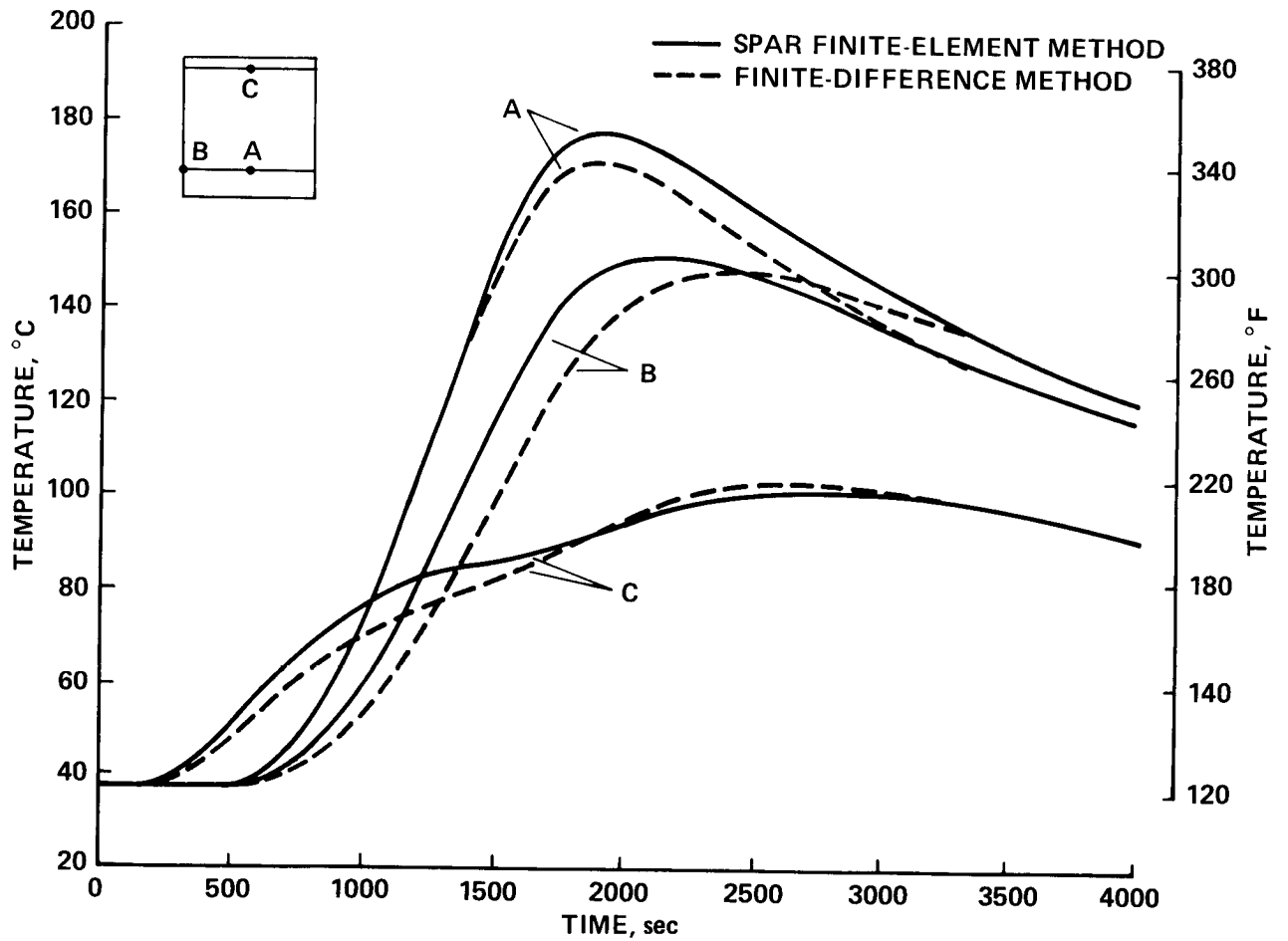


Figure 40. Comparison of WS240 bay 3 structural temperatures predicted by SPAR finite-element method and finite-difference method for two-dimensional one-cell model (Rockwell mission 3 heating).

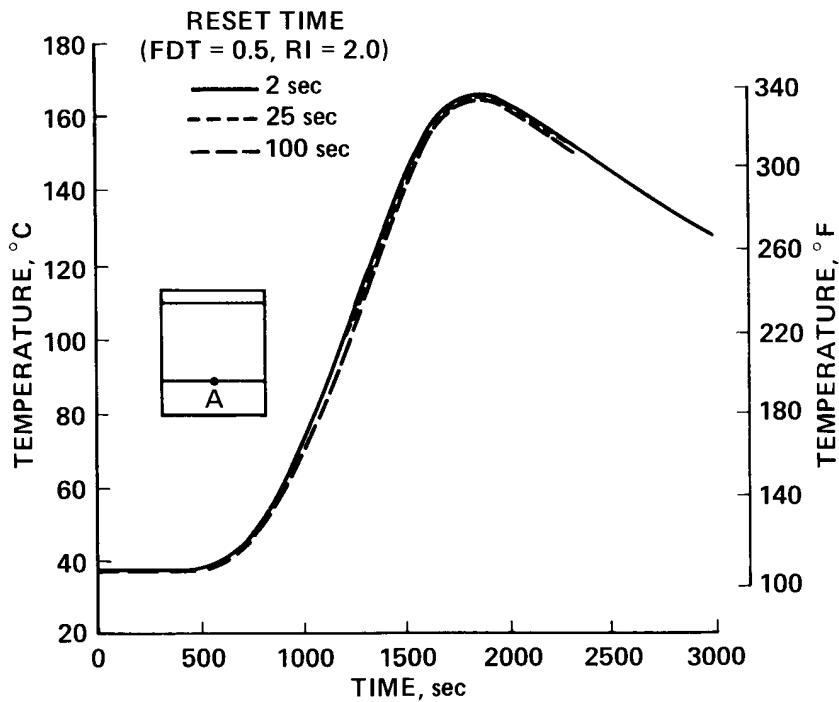


Figure 41. Aluminum lower skin temperatures for WS240 bay 3, predicted from different values of SPAR RESET TIME for three-dimensional one-cell model (Rockwell mission 3 heating).

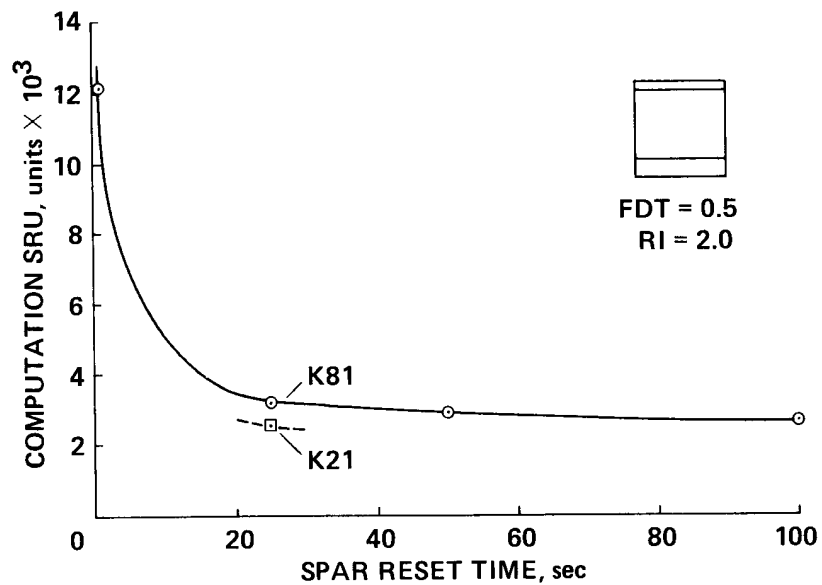


Figure 42. Computer SRU units for various values of SPAR RESET TIME for WS240 bay 3 three-dimensional one-cell model (Rockwell mission 3 heating).

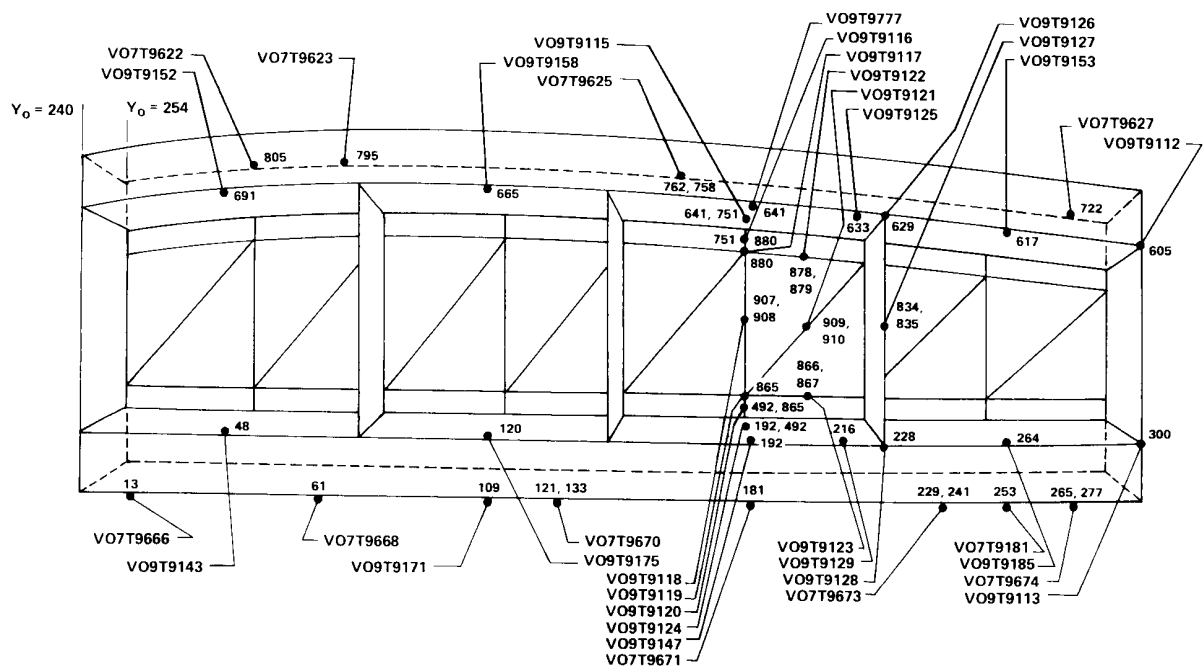


Figure 43. Thermocouple locations on WS240. (Smaller numerals indicate JLOC numbers.)

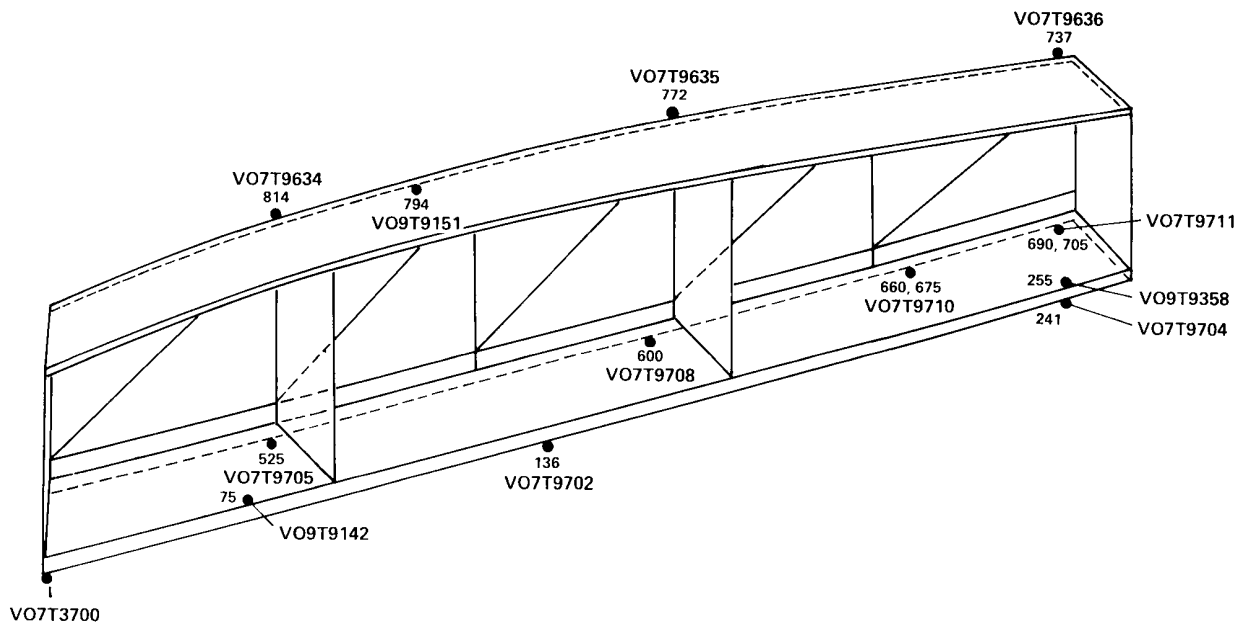


Figure 44. Thermocouple locations on WS328. (Smaller numerals indicate JLOC numbers.)

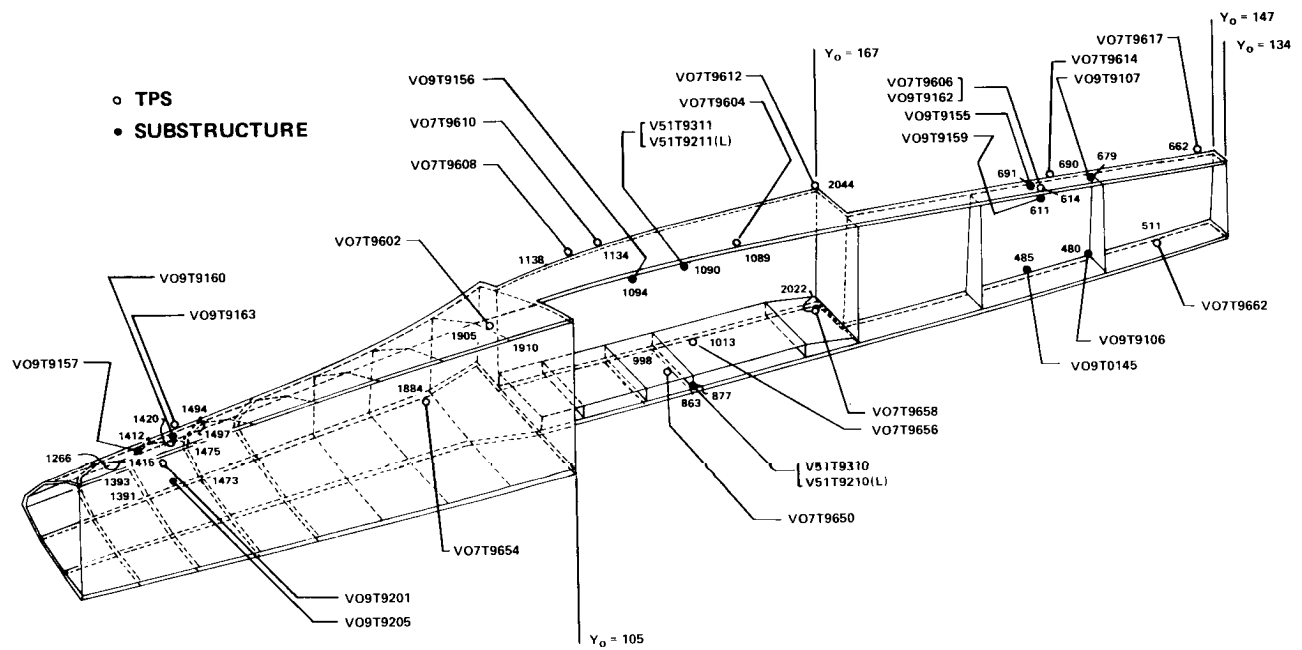


Figure 45. Thermocouple locations on WS134. (Smaller numerals indicate JLOC numbers.)

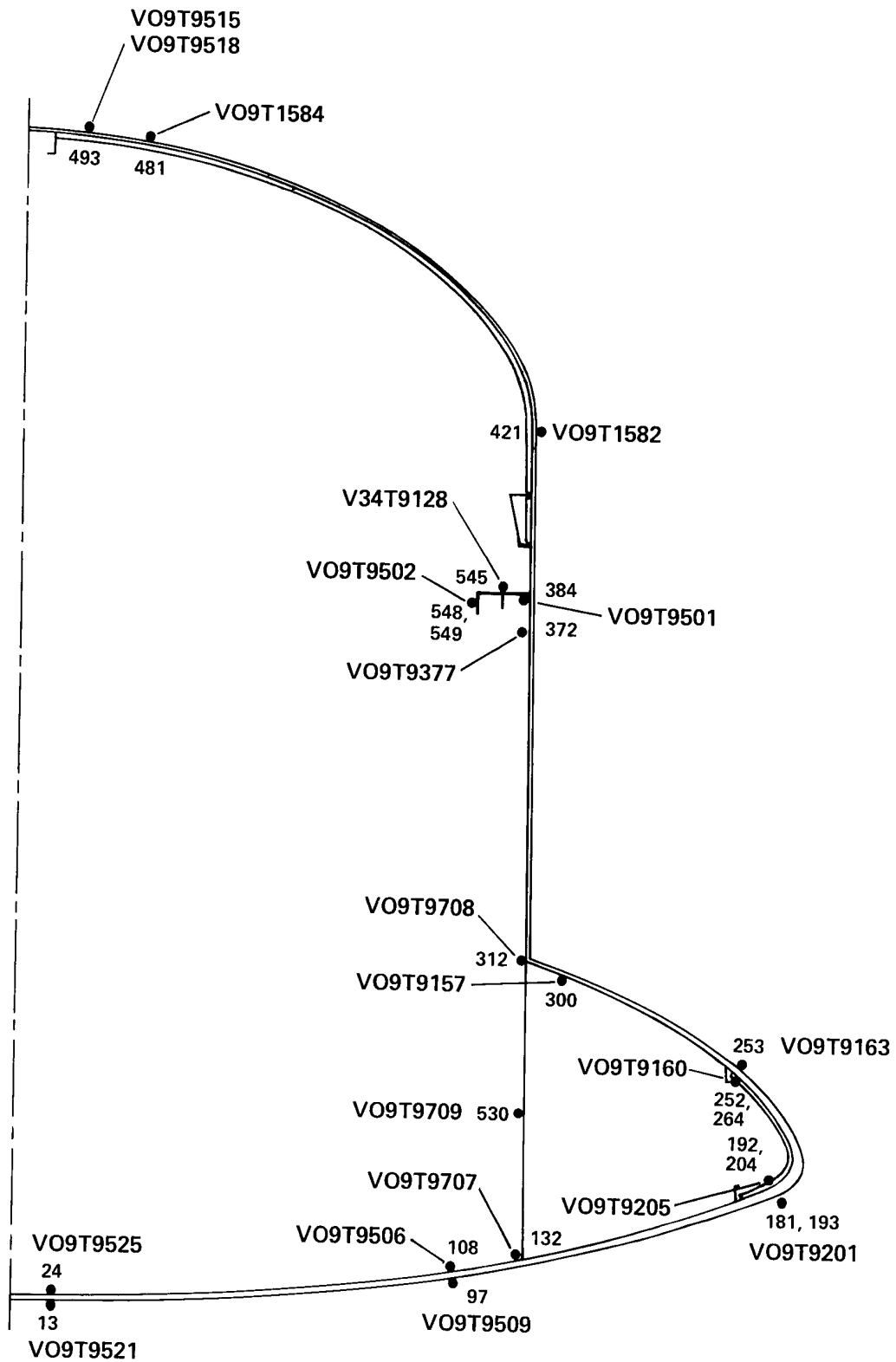


Figure 46. Thermocouple locations on FS877. (Smaller numerals indicate JLOC numbers.)

